M 2026

U.PORTO
FEUP FACULDADE DE ENGENHARIA
UNIVERSIDADE DO PORTO

DEVELOPMENT OF HIGH-PERFORMING ELECTRODES FOR VANADIUM REDOX FLOW BATTERIES

MARTA MARIA PINHEIRO GARCIA BARRETO ARCHER
MASTER'S DISSERTATION IN CHEMICAL ENGINEERING
PRESENTED TO THE FACULTY OF ENGINEERING
OF THE UNIVERSITY OF PORTO

Master in Chemical Engineering

Development of high-performing electrodes for vanadium redox flow batteries

Master's Dissertation

of

Marta Maria Pinheiro Garcia Barreto Archer

Developed within the scope of the Dissertation course unit

held in

LEPABE – Laboratory for Process Engineering, Environment, Biotechnology and Energy



Supervisor at FEUP: **Yuliya Ivanova**

Joint supervisor at FEUP: **Prof. Adélio Mendes**

FACULTY OF ENGINEERING OF THE UNIVERSITY OF PORTO

DEPARTMENT OF CHEMICAL AND BIOLOGICAL ENGINEERING

August 2026

Acknowledgment

Thank you to my supervisor, Dr. Yuliya Ivanova, for her guidance throughout this dissertation. Thank you for your kindness, patience and for always being so generous with your time.

I would also like to thank my co-supervisor, Professor Adélio Mendes, for the opportunity to carry out this work, and everyone at LEPABE who contributed, directly or indirectly, through their help and support during this project.

I would also like to thank my family for their love and support throughout this journey. A special thank you to my mom for always being my safe place. To my grandfather, thank you for lending me your strength when I needed it and to Hulk for teaching me to find joy in every day.

To my friends, thank you for making this journey lighter. A special thank you to Alexandra, my friend of every hour, for always helping me see things with clarity and for reminding me that everything always work out in the end.

And to Kiko, thank you for never letting me go through this journey alone. Somehow, the weight of every challenge always seemed lighter because you were there to share it. I could not have done it without you.

Institutional Acknowledgments

This work was supported by national funds through FCT/MECI: LEPABE, UID/00511/2025 (https://doi.org/10.54499/UID/00511/2025) and UID/PRR/00511/2025 (https://doi.org/10.54499/UID/PRR/00511/2025) and ALiCE, LA/P/0045/2020 (https://doi.org/10.54499/LA/P/0045/2020).

Abstract

Vanadium redox flow batteries (VRFBs) are among the most promising technologies for large-scale stationary energy storage, owing to their independent power and energy scaling, long cycle life, and safety, relevant for integrating renewable energy into the grid. However, for widespread deployment and further increasing the attractiveness of VRFB, improvements in energy efficiency at higher currents are required, which can be achieved by enhancing the electrochemical performance of carbon felt electrodes.

This work aimed to develop and evaluate surface modification strategies to improve the electrochemical performance of commercial carbon felt electrodes (SGL Sigracell GFD), targeting an energy efficiency (EE) of at least 80 % at 150 mA cm^{-2}. Thermal, chemical, and plasma treatments were investigated, individually and combined: thermal treatment (400–600 °C, varying durations); acid pre-treatment in sulfuric acid followed by thermal activation; a thermal–acid–thermal sequence; propylene conditioning; bismuth electrodeposition; and plasma treatment. Felts were characterized by conductivity under compression; the electrodes' electrochemical activity was assessed by cyclic voltammetry, electrochemical impedance spectroscopy, polarization curves, and galvanostatic cycling in a single flow cell. Replacing the anion-exchange membrane (FAPQ 330) with a cation-exchange membrane (Nafion NR-211) was also evaluated, and the best electrode treatment was upscaled from 4 cm^2 to 20 cm^2 active area.

Thermal treatment at 450 °C for 12 h gave the most conductive, active felts, yielding 80.09 % EE (Energy Efficiency) at 150 mA cm^{-2}. Adding a prior acid step (12 h in H_2SO_4) improved kinetics and lowered ohmic and charge-transfer resistances, giving the best performance: 99.11 % coulombic efficiency (CE), 83.26 % voltage efficiency (VE), and 82.52 % EE at 150 mA cm^{-2}. The alternating chemical thermal sequence, plasma treatment, propylene conditioning, and bismuth electrodeposition did not improve these metrics, either raising resistances and/or reducing V(II)/V(III) reversibility. Nafion NR-211 lowered CE but slightly raised VE via lower ohmic losses. Upscaling to 20 cm^2 yielded 79.7 % EE at 150 mA cm^{-2}. These results establish acid-first chemical–thermal treatment as an effective, scalable strategy for improving carbon felt electrodes, providing guidelines for high-performing VRFBs.

Keywords: vanadium redox flow batteries; carbon felt electrodes; surface treatment; energy efficiency; electrochemical characterization

Resumo

As baterias redox de escoamento de vanádio (VRFB) são das tecnologias mais promissoras para o armazenamento estacionário de energia em larga escala, devido ao dimensionamento independente da potência e da energia, à longa vida útil e à segurança, características relevantes para integrar energias renováveis na rede elétrica. No entanto, a implementação generalizada das VRFB continua limitada por eficiências energéticas moderadas, condicionadas pelo desempenho eletroquímico dos elétrodos de feltro de carbono, cuja superfície original apresenta atividade catalítica e molhabilidade limitadas face às reações redox do vanádio.

Este trabalho teve como objetivo desenvolver e avaliar estratégias de modificação superficial para melhorar o desempenho eletroquímico de elétrodos de feltro de carbono comerciais (SGL Sigracell GFD), visando uma eficiência energética (EE) de pelo menos 80 % para 150 mA cm^{-2}. Foram estudados tratamentos térmicos, químicos e por plasma, isolados ou combinados: tratamento térmico (400–600 °C, diferentes durações); pré-tratamento em ácido sulfúrico seguido de ativação térmica; uma sequência térmico–ácido–térmico; estabilização em propileno; eletrodeposição de bismuto; e tratamento por plasma. Os feltros foram caracterizados quanto à condutividade sob compressão; os elétrodos foram avaliados por voltametria cíclica, espetroscopia de impedância eletroquímica, curvas de polarização e ciclos galvanostáticos numa célula de escoamento única. Avaliou-se ainda a substituição da membrana aniónica (FAPQ 330) por uma catiónica (Nafion NR-211), e a melhor configuração foi escalada de 4 cm^2 para 20 cm^2 de área ativa.

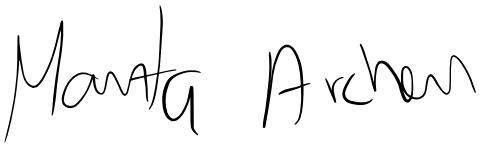
O tratamento térmico a 450 °C durante 12 h permitiu obter os feltros mais condutores e ativos, com EE de 80,09 % a 150 mA cm^{-2}. Um pré-tratamento ácido prévio (12 h em H_2SO_4) melhorou a cinética e reduziu as resistências ómica e de transferência de carga, dando o melhor desempenho: CE de 99.11 %, VE de 83.26 %, EE de 82.52 % a 150 mA cm^{-2}. A sequência em alternância química e térmica, o plasma, o propileno e o bismuto não superaram este resultado, cada um aumentando resistências e/ou reduzindo a reversibilidade do par V(II)/V(III). A Nafion NR-211 reduziu a CE mas melhorou ligeiramente a VE por menores perdas ómicas. O *upscale* para 20 cm^2 atingiu 79.7 % de EE a 150 mA cm^{-2}. Estes resultados estabelecem o tratamento químico–térmico com ácido em primeiro lugar como uma estratégia eficaz e escalável, fornecendo diretrizes para elétrodos de alto desempenho em VRFB.

Palavras-chave: baterias redox de escoamento de vanádio; elétrodos de feltro de carbono; tratamento de superfície; eficiência energética; caracterização eletroquímica

Declaration

I hereby declare, under word of honour, that this work is original and that all non-original contributions is indicated and due reference is given to the author and source

Sign and date



6th of July 2026

Index

1. Introduction 1

1.1. Framing and presentation of the work 1

1.2. Contribution of the author to the work 1

1.3. Organization of the dissertation 2

2. Context and State of the art 3

2.1. Electrical Energy Storage Technologies 3

2.1.1. Overview of Storage Technologies 3

2.1.2. Why Flow Batteries For Grid Scale 4

2.2. Redox flow batteries 4

2.2.1. Working Principle 4

2.2.2. RFB Chemistries 4

2.3. Vanadium Redox Flow Batteries (VRFBs) 5

2.3.1. Electrochemistry 5

2.3.2. Advantages and challenges 6

2.4. VRFB components 7

2.4.1. VRFB architecture 7

2.4.2. Electrolyte 7

2.4.3. Ion exchange membranes 7

2.4.4. Bipolar plates 8

2.4.5. Carbon felt electrodes 8

2.5. Characterization methods 11

2.5.1. Electrical conductivity 11

2.5.2. Cyclic voltammetry (CV) 11

2.5.3. Electrochemical impedance spectroscopy (EIS) and Polarization Curves 12

2.5.4. Battery cycling 13

2.6. Research gap and thesis objectives 14

3. Materials and Methods 15

3.1. Materials 15

3.2. Electrode Preparation and Surface Treatments 15

3.2.1. Felt Electrode Preparation 15

3.2.2. Thermal Treatment of Electrodes 15

3.2.3. Chemical Treatment 16
3.2.4. Combined and Sequential Treatments 16
3.2.5. Plasma Treatment 16
3.2.6. Bismuth Electrodeposition 16
3.2.7. Post-Treatment Stabilization in Propylene Atmosphere 17
3.3. Experimental Setup 17
3.3.1. Single-Cell Configuration 17
3.3.2. Electrolyte Circulation System 18
3.3.3. Measurement and Control Equipment 18
3.4. Electrochemical Testing Procedures 18
3.4.1. Electrical Conductivity Measurements 18
3.4.2. Cyclic Voltammetry 18
3.4.3. Electrochemical Impedance Spectroscopy and Polarisation Measurements 19
3.4.4. Charge–Discharge Cycling 19
3.4.5. Scanning electron microscopy with energy-dispersive X-ray spectroscopy (SEM-EDS) .. 20
4. Results and discussion 21
4.1. Effect of thermal treatment (temperature and duration, combined) 21
4.1.1. Electrical conductivity 21
4.1.2. EIS Results 22
4.1.3. Battery cycling performance 23
4.2. Chemical pre-treatment (acid-first) combined with thermal 24
4.2.1. CV analysis 24
4.2.2. EIS Results 25
4.2.3. Polarization Results 27
4.2.4. Battery cycling performance 28
4.2.5. Alternating Thermal–Chemical Sequence (Thermal–Acid–Thermal) 29
4.3. Plasma treatment 30
4.3.1. EIS Results 30
4.3.2. Polarization results 31
4.3.3. Battery cycling performance 32
4.4. Post-Treatment Conditioning in Propylene Atmosphere 33
4.4.1. CV analysis 33

4.4.2. EIS Results 34
4.4.3. Polarization results 35
4.4.4. Battery cycling performance 35
4.4.5. Discussion 36
4.5. Bismuth electrodeposition 36
4.5.1. CV analysis 36
4.5.2. EIS Results 37
4.5.3. Polarization results 38
4.5.4. Battery cycling performance 38
4.5.5. SEM analysis 39
4.6. Performance of flow cell with conventional cationic exchange membrane 40
4.6.1. EIS Results 40
4.6.2. Polarization results 41
4.6.3. Battery cycling performance 42
4.7. Upscaling 42
5. Conclusions 44
6. Assessment of the work done 46
6.1. Objectives Achieved 46
6.2. Contribution to the Sustainable Development Goals 46
6.3. Final Assessment 46
7. References 48
Appendix A - Comparison of Energy Storage Technologies 51
Appendix B - Comparison of non-vanadium redox flow battery chemistries 52
Appendix C - Parameter tables for 4.65EA Sigracell felt and FAPQ 330 and Nafion 211 membranes 54
Appendix D - SEM Micrographs of Untreated and Treated Carbon Felt Electrodes 55
Appendix E - Consolidated Cycling Performance Across All Treatment Conditions 56
Appendix F - Python-Based Data Processing Scripts 57
cv_analysis.py — Cyclic Voltammetry Peak and Charge Analysis 57
Scan Rate and Electrode Area 57
Peak Detection and Baseline Correction 57
Peak-Derived Metrics 58
Onset Potential 58
vrfb_cycles.py — Cycling Performance Calculations 59

Coulombic Efficiency 59

Voltage and Energy Efficiency — Approximate (log-based)..... 59

Voltage and Energy Efficiency — Exact (timeseries-integrated)..... 59

Anomaly Flagging 60

polarization_analysis.py — Polarization Curve Metrics 61

Appendix G - Cycling metrics for battery using Bismuth modified felt..... 63

Appendix H - SEM picture and spectrum for bismuth modified felt..... 64

List of Figures

Figure 1: Generalized polarization curve for a VRB indicating the dominant source of overpotential in each region [30] 13

Figure 2: Image of the assembled single flow cell employed in the work. 17

Figure 3: Effect of compression level of felt samples on the electric conductivity. 21

Figure 4: Nyquist plots obtained for the flow cell assembled with felt electrodes treated at different conditions (a) (left) Temperature series (untreated, 400 °C, 450 °C, and 500 °C, all at 12 h). (b) (right) Duration series at 450 °C (6, 12, and 24 h). 22

Figure 5: Cyclic voltammograms recorded at felt electrodes in the electrolyte containing V^{2+}/V^{3+} redox pair: (a) felt electrodes differing in duration of acid pretreatment step – no pretreatment, 3, 7, 12 and 18 h, (b) felt electrodes treated in acid for 12 h, and further at 400 ºC or 450 ºC for 12 h. 25

Figure 6: Nyquist plots for felt electrodes after different treatments: (a) acidic treatment duration (3, 7, 12, 18 h), (b) 12 h acid + thermal at 400/450°C vs. thermal-only at 450°C. 26

Figure 7: Polarization and power-density curves for acid-first treatments across acid-soak durations and thermal-step temperature..... 27

Figure 8: Nyquist plots recorded for flow cells assembled with felt electrodes subjected to different activation procedures: baseline acid treatment followed by thermal activation, and additional N_2 plasma treatment for different durations...... 30

Figure 9: Polarization and Power Density curves recorded for single cells assembled with felt electrodes subjected to different treatment procedures, the conditions are indicated on the plot ... 31

Figure 10: Cyclic voltammograms of the V^{2+}/V^{3+} couple recorded at felt electrodes after different treatment procedures: propylene conditioning vs. acid-first baseline..... 33

Figure 11: Nyquist plots for flow cells assembled with felt electrodes after different treatment procedures: propylene conditioning vs. acid-first baseline 34

Figure 12: Polarization and power-density curves, propylene-conditioned electrodes vs. acid-first baseline..... 35

Figure 13: Cyclic voltammograms of the V^{2+}/V^{3+} couple, bismuth-electrodeposited electrode vs. acid-first baseline..... 36

Figure 14: Nyquist plots, bismuth-electrodeposited electrode vs. acid-first baseline..... 37

Figure 15: Polarization and power-density curves, bismuth-electrodeposited electrode vs. acid-first baseline..... 38

Figure 16: Backscattered-electron micrographs of the bismuth-modified felt. (a) (left) overview, (b) (middle) higher-magnification detail, (c) (right) Threshold overlay (red) of the analysis in Fig. 16(a) 39

Figure 17: Nyquist plots, FAPQ 330 vs. Nafion NR-211 membranes 40

Figure 18: Polarization and power-density curves, FAPQ 330 vs. Nafion NR-211 membranes..... 41

Figure 19: Cycling performance of acid-first-treated electrodes at 20 cm^2 scale, 150–225 mA cm^{-2}, Pinflow cell 43

Figure 21: SEM micrograph of the untreated carbon felt 55

Figure 20: SEM micrograph of the thermal-only treated carbon felt (450 °C / 12 h) 55

Figure 22: SEM micrograph of the acid-first treated carbon felt (H_2SO_4 / 12 h - 450 °C / 12 h)..... 55

Figure 23: Schematic cyclic voltammogram (illustrative, not measured data) showing the anodic and cathodic peaks and the quantities derived from them. 59

Figure 24: SEM micrograph of the bismuth modified felt surface 64

Figure 25: EDX spectrum of the bismuth deposit on the felt surface 64

List of Tables

Table 1: Thermal treatment matrix: temperature and dwell time combinations tested..... 16

Table 2: Summary of combined and sequential surface treatment conditions..... 16

Table 3: EIS-derived ohmic and charge-transfer resistance across the thermal screening matrix 22

Table 4: Cycling performance across the thermal screening matrix (150 mA cm $^{-2}$, reference cycle)... 23

Table 5: CV peak separation and peak current ratio for the V^{2+}/V^{3+} couple, acid-first treatments.... 25

Table 6: EIS-derived ohmic and charge-transfer resistance for acid-first treatments 26

Table 7: Polarisation metrics for acid-first treatments 27

Table 8: Cycling performance of cells with felt electrodes treated at different acid-soak durations prior to 450 °C–12 h thermal treatment (150 mA cm $^{-2}$, reference cycle)..... 28

Table 9: Cycling performance of acid-first treatment (H_2SO_4, 12 h) at 400 °C vs. 450 °C thermal step (150 mA cm $^{-2}$, reference cycle) 29

Table 10: EIS-derived ohmic and charge-transfer resistance for plasma-treated electrodes vs. acid-first baseline..... 31

Table 11: Polarization metrics for plasma-treated electrodes vs. acid-first baseline 32

Table 12: Cycling performance for plasma-treated electrodes vs. acid-first baseline (150 mA cm $^{-2}$, reference cycle) 32

Table 13: CV peak separation and peak current ratio for the V^{2+}/V^{3+} couple at felt electrodes after different treatment procedures 34

Table 14: EIS-derived ohmic and charge-transfer resistance for propylene-conditioned electrodes vs. acid-first baseline..... 34

Table 15: Polarization metrics for propylene-conditioned electrodes vs. acid-first baseline..... 35

Table 16: Cycling performance for propylene-conditioned electrodes vs. acid-first baseline (150 mA cm $^{-2}$, reference cycle) 35

Table 17: CV peak separation and peak current ratio for the V^{2+}/V^{3+} couple, bismuth-electrodeposited electrodes vs. acid-first baseline 37

Table 18: EIS-derived ohmic and charge-transfer resistance for bismuth-electrodeposited electrodes vs. acid-first baseline..... 37

Table 19: Polarization metrics for bismuth-electrodeposited electrodes vs. acid-first baseline..... 38

Table 20: Cycling performance of cells with bismuth-electrodeposited electrodes vs. acid-first baseline (150 mA cm $^{-2}$, reference cycle)..... 38

Table 21: IS-derived ohmic and charge-transfer resistance, FAPQ 330 vs. Nafion NR-211 membranes . 41

Table 22: Polarization metrics, FAPQ 330 vs. Nafion NR-211 membranes 41

Table 23: Cycling performance, FAPQ 330 vs. Nafion NR-211 membranes (150 mA cm $^{-2}$, reference cycle) 42

Table 24: Contribution to the Sustainable Development Goals 46

Table 25: Comparison of energy storage technologies by key performance metrics [5], [7], [8]..... 51

Table 26: Comparison of non-vanadium redox flow battery chemistries [7], [9], [10], [34], [35], [36], [37]..... 52

Table 27: Physical properties of SGL Sigracell GFD 4.65 EA carbon felt 54

Table 28: Specifications of the FAPQ 330 and Nafion NR-211 membranes..... 54

Table 29: Mean Coulombic, voltage, and energy efficiencies (cycles 2–5) across all treatment conditions tested (150 mA cm $^{-2}$)..... 56

Table 30: Automatic anomaly-flagging criteria (defaults). 61

Table 31:Efficiency metrics for battery using Bi-modified felt 63

Notation and Glossary

A	Geometric (active) electrode area	cm^2
C	Bulk concentration of the redox species (Randles–Ševčik equation)	mol cm^{-3}
CE	Coulombic efficiency	%
C_{dl}	Double-layer capacitance	F (or F cm^{-2})
D	Diffusion coefficient	cm^2 s^{-1}
E	Cell / electrode potential	V
EE	Energy efficiency	%
F	Faraday's constant	C mol^{-1}
i_p	Peak current	A (or mA)
i_{pa}, i_{pc}	Anodic / cathodic peak current	A (or mA)
j	Current density	mA cm^{-2}
L	Felt thickness	mm
n	Number of electrons transferred	dimensionless
P_d	Power density	mW cm^{-2}
Q	Total charge passed, per half-cycle, by integration of current	C (or mA h)
R	Universal gas constant	J mol^{-1} K^{-1}
R	Electrical resistance	Ω
R_{ct}	Charge-transfer resistance	Ω (or Ω cm^2)
R_s	Solution / series resistance	Ω (or Ω cm^2)
T	Absolute temperature	K
v	Scan rate	mV s^{-1}
VE	Voltage efficiency	%
Z, Z', Z''	Complex impedance; real part; imaginary part	Ω

Greek Letters

Δ	Difference operator
ΔE_p	Peak-to-peak separation
ω	Angular frequency

Indexes

a	Anodic
c	Cathodic
ct	Charge-transfer
dl	Double-layer
s	Solution

List of Acronyms

AC	Alternating Current
AEM	Anion Exchange Membrane
CAES	Compressed Air Energy Storage
CPE	Constant Phase Element
CSV	Comma-Separated Values
CV	Cyclic Voltammetry
DC	Direct Current
EIS	Electrochemical Impedance Spectroscopy
IEC	Ion Exchange Capacity

OCP	Open-Circuit Potential
PHS	Pumped Hydro Storage
PTFE	Polytetrafluoroethylene
R&D	Research and Development
RFB	Redox Flow Battery
SHE	Standard Hydrogen Electrode
SOC	State of Charge
UPS	Uninterruptible Power Supply
USD	United States Dollar
VRFB	Vanadium Redox Flow Battery

1. Introduction

1.1. Framing and presentation of the work

The world is changing, and it is changing at a much faster pace than previously anticipated. Growing geopolitical tensions and climate-related phenomena compel countries worldwide to intensify their efforts toward the energy transition and, above all, to strengthen their energy independence.

In less than one year, Portugal has faced two major stress tests, surrounding its energy system. The first incident was on the 28th of April 2025. It was the Iberian blackout that disrupted the energy supply across Portugal, leaving the country in the dark for several hours. According to REN (National Energy Networks) [1], the event may have been linked to a significant voltage oscillation originating in Spain and propagating into Portugal. The second incident was storm Kristin, which caused extensive damage on the distribution infrastructure, leading to outages that left the country's central region without electricity or communications for weeks [2].

While storms cannot be prevented, energy solutions can help mitigate their impacts by strengthening local resilience and ensuring continuity of critical services. On the other hand, the blackout highlighted one of the key vulnerabilities in interconnected systems: cross-border disturbances. A more self-reliant system could have reduced Portugal's exposure to external fluctuations and mitigated, or potentially avoided, the disruption.

Moreover, at the 2026 World Economic Forum in Davos, Prime Minister of Canada Mark Carney called on "middle powers" to coordinate and innovate so they are not forced into dependence on unstable external sources of strategic goods and energy [3]. Against this backdrop, energy storage becomes a key enabling technology for resilience and energy sovereignty.

1.2. Contribution of the author to the work

The work presented in this dissertation was developed under the scientific supervision of the thesis supervisors and using the experimental facilities available in the laboratory. Within this framework, I was responsible for the design and execution of the experimental work aimed at improving the electrochemical performance of felt electrodes used in vanadium redox flow batteries (VRFBs).

The main objective of my work consisted in studying the influence of surface modification treatments applied to the commercial carbon felt materials on their performance as electrodes in VRFB. To achieve this objective, I defined the main treatment parameters, designed the experimental matrix, carried out the felt treatments, and performed their structural and electrochemical characterization. I also assembled the redox flow cells with the developed electrodes and evaluated their electrochemical performance. Furthermore, I was responsible

for processing and analyzing the experimental data, including assessing the effects of the electrode treatments on their morphology, electrical properties, and electrochemical behavior in a three-electrode configuration, as well as their overall performance in a redox flow cell. The latter included electrochemical impedance measurements, current and power density analyses, and the determination of charge–discharge efficiencies through galvanostatic cycling tests.

Overall, my contribution to this work includes the definition of the experimental methodology, the preparation and treatment of the electrode materials, the execution of the electrochemical tests, and the analysis and interpretation of the experimental results presented in this dissertation.

1.3. Organization of the dissertation

The first chapter introduces the dissertation, framing the work within the context of energy storage and energy security, and presents the author's contribution to the experimental work described in the following chapters.

The second chapter presents a literature review of energy storage technologies and redox flow batteries, focusing on vanadium redox flow batteries and the improvement of highly performing carbon felt electrodes, and concludes by identifying the research gap and objectives addressed by this work.

The third chapter describes the materials, electrode surface treatments, and experimental setup used, along with the electrochemical testing procedures and performance metrics applied throughout the work.

The fourth chapter presents and discusses the results obtained for each surface treatment investigated, comparing their effect on electrode and cell performance.

The last two chapters summarize the main conclusions drawn from the experimental work and present an overall assessment of the objectives achieved.

2. Context and State of the art

2.1. Electrical Energy Storage Technologies

2.1.1. Overview of Storage Technologies

Storage technologies can be categorized into five groups based on their operating principles: mechanical, electrochemical, electrical, thermal, and chemical [4], [5]. No single technology universally outperforms the rest in every application. Hence, various technologies tend to be used in parallel, as it is infrequent that high power density, high energy density, low cost, and fast response time are achieved at the same time [6].

Pumped hydro storage (PHS) has dominated grid-scale storage over the years and has the most aggregate installation in the world due to the long operational lifetime (40–60 years) and round-trip efficiency of 70–85 % of its storage systems [4], [5]. This dominance has been in decline due to the rapid expansion of battery storage in the last decade [7]. In the context of mechanical energy storage, Compressed Air Energy Storage (CAES) occupies the same niche as PHS at smaller scales. CAES systems that are either adiabatic or isothermal can achieve round-trip efficiencies of 70–75 % [4], [5]. Both PHS and CAES face similar geographic and scale limitations at large site-specific installations.

Table 26 in Appendix A illustrates a limited selection of the technologies compared here; a wider comparison is found in [4], [5], [8]. In addition to the metrics in the table, a number of qualitative factors also allow differentiation. Lithium-ion batteries dominate the energy storage market; however, ong-term costs are uncertain due to supply chain concerns surrounding lithium and cobalt. Cobalt costs alone are around 900–1300 USD/kWh [5], [7], [8]. Sodium-sulphur batteries are kept near 300 °C to maintain the liquid state when in operation; this creates a burden of thermal management which is not captured in efficiency metrics. Vanadium redox flow batteries are structurally very different from the mentioned conventional systems. In VRFBs, the energy-sustaining electrolyte is external to the electrochemical cell. Therefore, in contrast to conventional batteries, energy and power can be independently designed and scaled [9], [10]. The VRFBs are especially suitable for long-duration, stationary applications.

2.1.2. Why Flow Batteries For Grid Scale

Table 26 also illustrates a gap in duration coverage. Lithium-ion batteries and supercapacitors are suited for short-burst, high-power applications, while pumped hydro and CAES address long-duration storage but only at specific sites with suitable geography. A highly renewable grid requires duration flexibility that neither group can offer without site constraints.

Flow batteries fill this gap because their system's energy-to-power ratio can be tailored to the duration required by a given application, rather than being fixed by the choice of cell chemistry, by simply changing the volume of electrolyte stored in the external tanks [4]. This flexibility is the central reason flow batteries are considered for long-duration, site-independent grid storage, and motivates the closer examination of redox flow battery (RFB) operating principles and chemistries that follows.

2.2. Redox flow batteries

2.2.1. Working Principle

One of the important differences between RFBs and other conventional batteries is that RFBs use liquid electrolytes to store energy as opposed to solid electrolytes and electrodes [9], [10]. In RFBs, the anolyte and the catholyte are each contained in separate external storage tanks outside of the electrochemical cell and are pumped through a cell stack, where they flow through a pair of porous electrodes separated by an ion exchange membrane. During the discharging of the battery, the species at the negative electrode of the battery undergoes oxidation and send electrons to the external circuit. Those electrons are then consumed in a redox reaction at a positive electrode. At discharge, the reverse redox reactions occur. The membrane does not take part in any of the electron transfer processes described. The coupling of the ion transport pathway (through the membrane) and the electron transport pathway (through the external circuit) is the defining structural feature of RFBs.

2.2.2. RFB Chemistries

The flow battery design presented earlier is generic and can be adapted to the specific chemistry employed, which determines multiple aspects of the system, such as cell voltage, energy density, performance stability, cost of active materials, and susceptibility to degradation mechanisms. The all-vanadium system, employing vanadium electrolyte, currently holds the most commercial viability and dominates the market of RFBs, However, there are other chemistries in the stage of commercialization or close to it, including all iron, iron-chromium, zinc-bromine, organic chemistries, and others. Some of them are listed in Table 27 in Appendix B.

2.3. Vanadium Redox Flow Batteries (VRFBs)

This technology traces its beginnings to the mid-1980s at the New South Wales University of Australia. Skyllas-Kazacos and Grossmith (1987) showed that in aqueous solutions of sulfuric acid, vanadium, which is capable of existing in four oxidation states, can be used at both electrodes. Since both solutions are of the same element in different oxidation states, the cross-contamination through the membrane does not permanently damage the system. This is because the element that crosses is compatible with the electrolyte it enters, and the system can be restored by rebalancing. This contribution solved one of the major problems of the other flow battery chemistries and allowed for the development of a system that operates for a long time [10], [11].

2.3.1. Electrochemistry

At the negative electrode, during the charge process, V(III) in the negative electrolyte is reduced to V(II) by gaining an electron from the external circuit:

$$\mathrm{V^{3+}} + e^- \rightarrow \mathrm{V^{2+}} \qquad E^\circ = -0.26\ \mathrm{V}\ \textit{vs}\ \mathrm{SHE} \tag{1}$$

During the discharge process, the reverse of the charge process takes place, and V(II) is oxidized back to V(III).

At the positive electrode, during charging, VO^{2+} is oxidized to VO_2^+, while water participates in the reaction, releasing protons to the solution:

$$\mathrm{VO^{2+}} + \mathrm{H_2O} \rightarrow \mathrm{VO_2^+} + 2\mathrm{H^+} + e^- \qquad E^\circ = +1.00\ \mathrm{V}\ \textit{vs}\ \mathrm{SHE} \tag{2}$$

During the discharge process, VO_2^+ is reduced back to VO^{2+}, and an electron from the external circuit is received. The overall reaction of the cell can be expressed as the following:

$$\mathrm{V^{3+}} + \mathrm{VO^{2+}} + \mathrm{H_2O} \underset{\text{discharge}}{\overset{\text{charge}}{\rightleftharpoons}} \mathrm{V^{2+}} + \mathrm{VO2^+} + 2\mathrm{H^+} \qquad E^\circ\mathrm{cell} = 1.26\ \mathrm{V} \tag{3}$$

The standard open-circuit voltage of 1.26 V corresponds to the standard potentials of the pair of half-cell reactions. The actual potential during open-circuit conditions is not constant and varies with the state of charge of the electrolytes as well as with the concentration of ions in the solution. The actual potential is expressed by the full cell reaction Nernst equation:

$$E_{\mathrm{cell}} = E^\circ_{\mathrm{cell}} + \frac{RT}{F} \ln\left(\frac{[\mathrm{V^{2+}}][\mathrm{VO_2^+}][\mathrm{H^+}]^2}{[\mathrm{V^{3+}}][\mathrm{VO^{2+}}]}\right) \tag{4}$$

where R is the universal gas constant, T is temperature, and F is Faraday's constant. The open-circuit voltage in practice varies between 1.2 V at a low state of charge to 1.6 V when fully charged [9], [12].

2.3.2. Advantages and challenges

A key advantage of vanadium chemistry compared with other redox flow battery chemistries is that membrane crossover does not cause irreversible capacity loss. As vanadium is used as the active species in both half-cells, cross-contaminated electrolytes can be restored by remixing or rebalancing the electrolyte solutions, rather than replacing the active materials. Given the importance of long operational lifetime for reducing system cost and minimizing demand for critical materials, this characteristic further enhances the relevance of vanadium redox flow batteries. Therefore, electrolyte recovery and reuse have become essential considerations in the development and deployment of vanadium-based redox flow battery systems [7].

Because there is no solid-state electrochemical degradation in the vanadium system, its cycle life is rather high - between 10,000 and 20,000 cycles. This greatly exceeds what lithium-ion technologies can offer under deep-cycling conditions [7], [9]. Because the electrolyte is aqueous, the thermal runaway that occurs in lithium-ion systems is absent here. Therefore, VRFB systems can be installed in locations that are populous or sensitive to industrial activity [10], [13]. When the system is not actively cycling, self-discharge is minimal. This is the case, as long as the pumps are off and the electrolytes are not circulating. When the electrolytes are in separate tanks, there is no spontaneous chemical reaction. Therefore, the system is not self-discharging [7] and safe.

The reasons VRFBs have not economically challenged lithium-ion batteries in the energy storage market can be found in their drawbacks. In general, specific energy density in the vanadium systems does not reach more than 40 $Wh\,kg^{-1}$ with cell design and electrolyte concentrations consideration. The vanadium system struggles with the solubility of the vanadium and the cell operates with a lower cell voltage in comparison with a number of other chemistries, like lithium. The temperature also has a narrow operating range, between 10 and 40 °C, because of the precipitation of the vanadium compounds in the positive solution, which fails and causes damage to the system [7], [8]. The cost barrier to vanadium systems versus lithium-ion is irrefutable, thanks to the price of vanadium and the cost of the ion exchange membrane in the system which also increases costs. The efficiency of a VRFB system is still lower than that of lithium-ion systems [7], [14]. Improving this parameter is essential for increasing further the attractiveness and competitiveness of the VRFBs.

2.4. VRFB components

2.4.1. VRFB architecture

The fundamental building block of the VRFB system is the single electrochemical cell. This includes two felt electrodes (made from a porous form of carbon) which are separated by an ion exchange membrane. Each electrode is contained in a bipolar plate. The felt electrodes serve as a substrate for the vanadium redox reaction, and the bipolar plates gives the structural support for the electrode. The frames and gaskets are used to provide the required compression to the electrodes, create the path for the electrolyte inside the cell, and prevent leakage of the electrolyte from the cell. The membrane separates the two electrolyte streams while balancing the transport of protons through the cell.

A sufficient operating voltage for the application requires multiple cells to be physically arranged in series in a stack. Within the stack, the positive and negative electrolytes flow in parallel through the respective electrode compartments to each cell. A common manifold system distributes the electrolytes to the various cells. The power of the stack is defined by the number and the active size of the electrodes employed, while the energy density is defined by the amount of electrolyte used. The electrolyte circulation is provided by the pumps.

2.4.2. Electrolyte

The main components of aqueous vanadium electrolyte are vanadium species, with the concentrations in the range of 1.5 to 2.5 M, in the supporting electrolyte – sulphuric acid, with a concentration of 2 to 5 M [9].

A major challenge in practical applications is the stability of the vanadium electrolyte. The V^{2+} ions at the negative electrode can be oxidized by dissolved oxygen, and handling or cycling in air can lead to a loss of capacity. The positive electrolyte of V^{5+} is thermally unstable and can precipitate as V_2O_5. Therefore, the operating temperature of the vanadium system is limited to the range of 10–40 °C [7], [12]. Because both half-cell electrolytes contain vanadium, the state of charge of the system can be evaluated by the open-circuit voltage of the cell according to the Nernst equation, or by spectrophotometric methods used to quantify vanadium species in different oxidation states in solution [10].

2.4.3. Ion exchange membranes

The ion exchange membrane is located in the center of the cell. During charging and discharging, it should allow protons to flow between the half-cells to maintain charge balance. However, it should prevent vanadium ions in one of the electrolytes from crossing

to the other half cell. Vanadium crossover will lead to self-discharge and capacity loss. Because of that, minimizing crossover is a key factor in membrane selection. [10], [15]

Nafion, developed by DuPont, is a perfluorosulfonic acid membrane that dominates the field of membranes in VRFB due to its high chemical stability and high proton conductivity. However, cost and vanadium permeability, particularly V^{2+} and V^{3+}, make it a poor choice among the existing options of membranes [7], [15]. Anion exchange membranes have shown potential as a valid alternative. They are made of positively charged matrix polymer. Since they contain fixed positive charges, AEMs can repel positively charged vanadium ions and thus crossover is decreased. They typically have low proton conductivity. [9], [15]. Less expensive and more sustainable membranes, such as sPEEK membranes (sulphonated polyether ether ketone) or polybenzimidazole are also being developed [16].

2.4.4. Bipolar plates

Bipolar plates work as structural back support to the cell stack in addition to collecting current. The plates have to be designed to meet a number of specific requirements, such as good electrical through-plane conductivity, stability in the vanadium and sulfuric acid environment, low permeability to gases, and mechanical strength to withstand the assembly compressive loads [10], [12].

2.4.5. Carbon felt electrodes

2.4.5.1. Role and requirements

The function of the carbon felt electrode in a VRFB system is to offer a big surface area that is electrochemically active to a fast and selective vanadium redox reaction [10], [15]. An electrode should also have the ability to transport electrons to the bipolar plate, be stable in a strongly acidic, oxidizing environment for many electrochemical cycles. These challenges shape the properties the materials can have.

To reduce losses from electrical resistance, both in-plane and through-plane electrical conductivity need to be maximized. In addition, the mechanical and structural properties of the electrode materials must allow unimpeded electrolyte transport through the bulk of the electrode. One of the limitations in the performance of untreated carbon felt for VRFB applications is the material’s surface wettability. Poor wettability leads to a greater proportion of the felt's internal surface area not contacting the electrolyte during operation. This decreases the actively available surface area for electrochemical reactions and creates non-uniform electrolyte distribution and related non-uniformity in local current distribution over the surface. It also decreases voltage efficiency [15], [17]. Besides, the untreated carbon also has relatively low intrinsic catalytic activity for the redox pairs of vanadium. This is

particularly true for the V^{2+}/V^{3+} redox pair at the negative electrode, which is the reaction with the slowest kinetics in the VRFB [15], [18].

2.4.5.2. Commercial felts

The commercial carbon felt electrodes are manufactured using the thermal decomposition of precursor, rayon or polyacrylonitrile, in inert gas, producing a material with a disordered carbon structure, which has high surface energy and a moderate electrical conductivity. In the case of graphite felt, calcination takes place at temperatures that exceed 2000 °C. This causes the carbon felt's surface to become partially graphitic. In this case, the felt's electrical conductivity increases, but its surface energy decreases. The drawback is that, with a more graphitic structure and fewer surface defects, the felt becomes more difficult to treat and therefore more difficult to modify which limits the modification approaches and their effectiveness [15], [17].

The SGL Sigracell range from SGL Carbon is one of the most common commercial range used for academic VRFB research. The Sigracell range has different series and variations based on precursor type, thickness, and level of graphitization. The EA series are carbon felts produced from a polyacrylonitrile precursor, and have higher surface areas and good chemical stability [15], [19].

2.4.5.3. Surface treatment approaches

Untreated carbon felts have many limitations, therefore, a large number of surface treatment methods have been researched. The objective of these methods has been to develop surface treatments that introduce oxygen functional groups that improve wettability and create more electrocatalytic active sites for the vanadium redox couples. The most common surface treatment methods have been thermal and chemical oxidation, as well as treatment with plasma.

Of the methods available, heating carbon felt within an oxidizing atmosphere is perhaps the easiest to deploy, and the most mentioned in literature. Generally, oxidizing is realized in air at temperatures between 300 and 600 °C, for minutes to several hours. During this process some carbon is consumed, and reactive surface oxygen is introduced in functional surface groups like hydroxyl (C–OH), carbonyl (C=O), and carboxyl (–COOH) groups. The presence of these functional groups increases fiber surface energy and improve the wettability of the fibers. The carbonyl and carboxyl groups are believed to reduce the charge transfer resistance for the vanadium redox couples, and are also considered electrocatalytic sites [15], [18].

Among many parameters, treatment temperature stands out. Specifically, when treatment occurs below 350 °C, little oxidation occurs to enhance wettability and catalytic activity, while between 400–450 °C, numerous studies show that functional groups increase while

maintaining structural integrity of the fibers [19], [20], [21]. Conversely, carbon burnoff and fiber structure degradation occur above 500 °C. Due to the loss of electrical conductivity and mechanical strength, functional groups do not offset the negative effect on optimal structure [20], [22]. In addition to temperature, the treatment duration also affects the extent of oxidation. Beyond a certain duration, structural damages occurs instead of beneficial functionalization [23]. An additional factor that must be considered is the stability of thermally activated felts over time. In [24] it was showed that thermally treated felts stored in ambient air gradually lose wettability as surface contaminants from air adsorb on the activated surface. However, structural changes and oxygen functional groups are retained.

In chemical treatments, the felt is fully immersed within a liquid-phase oxidizing solution. The most commonly studied reagents include sulfuric acid, nitric acid and potassium permanganate [17], [25]. Using sulfuric acid as a treatment improves the hydrophilicity of the fibers and provides the formation of sulfonic and carboxylic groups through an oxidative attack. However, the trade-off between group density and structural integrity must be considered, with prolonged treatments resulting in significant degradation of the fiber. A combination of chemical and thermal treatments has been investigated in which the acid treatment is used to remove manufacturing residues and open the fibers. It is proposed that this provides a greater density of functional groups on the interior of the fibers than would be possible through thermal treatment alone [15], [18]. Carbon felt electrodes have also been modified through the deposition of nanoparticles, whether metallic, metal oxide, or other inorganic compounds, onto the fiber surface. Rather than functionalizing the existing carbon lattice through oxygen or nitrogen groups, this approach introduces a distinct catalytic phase that can directly enhance the kinetics of the vanadium redox couples [26].

Plasma treatment is a promising advance because it is faster, easier, and more reliable than other methods. A gas such as nitrogen, oxygen, or argon is excited into a plasma state, generating ions, radicals, and UV photons — reactive species that interact with the carbon surface to facilitate attachment of functional groups without requiring elevated temperatures. Plasma treatment can introduce nitrogen-containing groups like graphitic and pyridinic nitrogen, which are recognized as excellent sites for electrocatalytic activity. Similarly to thermal treatment, oxygen plasma also introduces oxygenated functional groups. Plasma treatment is extremely fast, and most methods only take a few seconds to minutes. Unlike other common methods, plasma treatment does not produce liquid waste. Unfortunately, as seen in the literature [27], [28], most of the effects from plasma treatment are seen on the outer surface of the felt fibers. This greatly limits the surface area that can become electroactive as treatment is most effective on thinner electrodes. Thick electrodes

will constrain the active surface area that can be achieved compared with thermal or chemical methods.

2.5. Characterization methods

2.5.1. Electrical conductivity

The most important type of conductivity of the felt is through-plane conductivity. This is because in an assembled cell, current will travel perpendicular to the electrode face. Current will flow from the reaction sites on the fiber surface, through the bulk of the felt and eventually to the bipolar plate and current collector. Through-plane conductivity can be calculated with the electrical resistance R of the felt, the compressed thickness of the felt denoted as L, and the cross-sectional area A of the bulk of the felt:

$$\sigma = \frac{L}{R \cdot A} \tag{5}$$

The measurement is done under controlled compression. This is due to the contact resistance and bulk resistance of the felt which are both dependent on the applied compression. To compare results across different treatments, the compression for each sample should be the same [20], [21]. The equipment and the compression protocol on which this work is based are detailed in Chapter 3.

2.5.2. Cyclic voltammetry (CV)

Cyclic voltammetry is a technique for studying the kinetics and reversibility of redox reactions. This is used as one of the methods for assessing the electrochemical performance of electrode materials in the catholyte and anolyte of the RFBs. The electrode is placed in a solution of the redox couple of interest. A triangular potential waveform is applied to a working electrode. The potential is scanned across a range, and the resulting current is measured.

The peaks observed at certain potentials correspond to the oxidation and reduction responses of the electroactive species. The shape, position, and size of the peaks help to study the electrochemical reaction kinetics and the reaction reversibility [15], [18].

In a reversible (or Nernstian) system, electron transfer is fast enough that the surface concentrations of the oxidized and reduced species remain in equilibrium with the applied potential at all times, following the Nernst equation. Under these conditions, the separation between the anodic and cathodic peak potentials remains close to the theoretical value of 59/n mV at 25 °C, n is the number of electrons transacted, independent of scan rate, and the peak current increases linearly with the square root of the scan rate, consistent with a diffusion-controlled process [29].

In a quasi-reversible system, the rate of electron transfer is comparable to the rate of mass transport, so the current is governed by both charge-transfer kinetics and diffusion. As a result, the peak-to-peak separation increases with increasing scan rate, and the shape and position of the voltametric peaks become dependent on the standard heterogeneous rate constant of the couple as well as on the scan rate itself. This behavior represents an intermediate case between the reversible and irreversible limits [29].

In an irreversible system, electron transfer is slow relative to the timescale of the experiment, so the surface concentrations no longer follow the Nernst equation. The voltammogram shows broader, more drawn-out peaks, larger peak separations, and, in the fully irreversible limit, the reverse peak may not appear at all, since the back-reaction becomes negligible on the timescale of the potential scan [29].

In cyclic voltammetry, the parameters ΔEp and the current peak ratio help classify the reversibility of a redox reaction. The peak separation can be computed using the equation:

$$\Delta Ep = \frac{59}{n} \tag{6}$$

The peak current ratio approaches 1.0 for fully reversible diffusion controlled systems. For quasi-reversible reaction systems, ΔEp is greater than the theoretical value and the peak current ratio will fall below 1.0. Surface treatment improves the electrode kinetics, thus reducing ΔEp, and yielding a peak current ratio that more closely approaches 1.0 [15], [18].

For the case of planar electrodes in a voltametric diffusion-controlled system, the peak current is described by the Randles-Ševčík equation.

$$i_p = 0.4463 \cdot n \cdot F \cdot A \cdot C \cdot \sqrt{\frac{n \cdot F \cdot D \cdot v}{R \cdot T}} \tag{7}$$

The equation includes terms for n the number of electrons, F Faraday's constant, A electrode area, C bulk concentration of the redox species, D diffusion coefficient, v scan rate, R the gas constant, and T the absolute temperature [12], [15].

2.5.3. Electrochemical impedance spectroscopy (EIS) and Polarization Curves

Electrochemical impedance spectroscopy (EIS) involves a small sinusoidal AC perturbation at different frequencies to capture the system's frequency-dependent electrical response. Because many processes in electrochemical cells, such as charge transfer, ohmic conduction and mass transport, are happening simultaneously but at different time scales, this allows them to be represented and analyzed individually as different impedance spectra in different ranges of frequencies [10], [15].

The data is commonly shown as a Nyquist plot, per which the negative imaginary data of complex impedance is plotted with respect to the real data across the span of frequency

measurements. A Bode plot, particularly its phase-angle representation, allows the phase shift between the applied voltage perturbation and the resulting current response to be visualized as a function of frequency.

A polarization curve, under steady-state or quasi-steady-state conditions, describes a cell's voltage output as a function of current density. This curve illustrates the effects of each type of cell loss, and the curve is particularly important as it describes the cell's operable power output capability at a given state of charge [10], [21].

A polarization curve usually shows three distinct sections. At low current densities, the voltage drop from the open-circuit value is predominately the result of activation overpotentials from the slow kinetics of the electrode reactions. For the intermediate region, a linear relationship between voltage and current density indicates ohmic losses. For the high current density region, the supply of reactants to the electrode surface becomes inadequate to allow the continuation of the applied current, and so a rapid voltage drop is seen. The scheme can be seen in Figure 1.

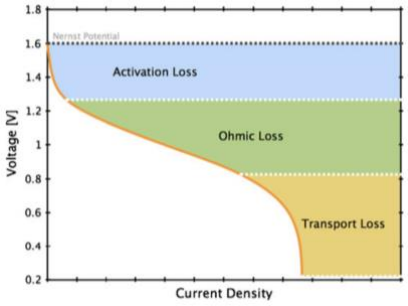


Figure 1: Generalized polarization curve for a RFB indicating the dominant source of overpotential in each region [30]

2.5.4. Battery cycling

For a direct assessment of a VRFB in operation, the best methodology is the galvanostatic charge-discharge cycling. Constant current charging is applied to the cell until a predetermined upper voltage limit is reached. The current is then reversed to discharge the cell until a predetermined lower voltage limit is reached. This is defined as one cycle, which is repeated in order to characterize the performance and the long-term stability of the system [10], [12].

From galvanostatic cycling, several performance metrics are obtained, including, voltage, coulombic and energy efficiencies (VE, CE, EE). These metrics indicate whether the performance has plateaued or whether degradation of the electrode or electrolyte has occurred during the galvanostatic cycling [15], [24].

CE reflects the fraction of charge recovered on discharge relative to charge input, and is degraded primarily by vanadium ion crossover through the membrane, which drives self-

discharge, and by parasitic side reactions, namely hydrogen evolution at the negative electrode and oxygen or CO_2 evolution at the positive electrode [31].

VE reflects the fraction of applied voltage recovered on discharge, and is constrained by three polarization sources: i) ohmic resistance across the electrolyte, membrane, felt, and contacts; ii) activation overpotential; and iii) mass-transport overpotential, which depends on felt porosity, wettability, and electrolyte flow [32]. Because EE is the product of CE and VE, it reflects these losses directly.

Details regarding current densities, voltage cutoffs, number of cycles, and data processing for this specific work are provided in Chapter 3.

2.6. Research gap and thesis objectives

Even though significant progress has been made in the development of VRFBs, several limitations still hinder their broader implementation, particularly in applications where higher efficiency and power performance are required.

Carbon felt electrodes are commonly used in VRFB systems because of their properties. However, in their untreated form, they show relatively low catalytic activity and limited wettability, both of which can restrict the efficiency of the vanadium redox reactions. A range of surface modification strategies, such as thermal, chemical, and plasma treatments, have been proposed to address these limitations. While these approaches often lead to performance improvements, the results reported in the literature are not always consistent, and in many cases depend strongly on the specific conditions under which the treatments are applied. Many works tend to focus on a single approach or a narrow set of parameters, which makes it difficult to draw broader conclusions or identify which strategies are genuinely more effective. In addition, the relationship between surface modifications, changes in physical properties (such as wettability or conductivity), and the resulting electrochemical performance are not always clearly established.

The present work aims to contribute to a structured understanding of how surface treatments influence behavior of carbon felt electrodes in VRFB systems. The main objective is to evaluate the effect of different modification strategies, with a particular focus on thermal treatments applied under varying conditions.

The performance of the treated electrodes will be assessed through characterization techniques, including conductivity measurements and electrochemical testing.

3. Materials and Methods

3.1. Materials

Carbon felt GFD 4.65 EA, from SGL Sigracell (SGL Carbon, Meitingen, Germany) was used as electrode material. The manufacturer provides the details of the porosity and thickness for this felt grade, along with areal weights, which are summarized in Table 27 in Appendix C. Fumasep FAPQ 330 anion exchange membrane from Fumatech bought from QuinTech was used as a separator. In selected tests, a Nafion NR-211 cation exchange membrane was used for comparison. Relevant specifications for the two membranes are provided in Table 28 in Appendix C.

Composite polymeric graphite PV15 (SIGRACELL, Germany) was used as bipolar plates.

The reagents H_2SO_4 (95-97 % w/w,JT Baker), HNO_3 (65 % w/w, Sigma Aldrich), $Bi(NO_3)_3 * 5H_2O$ (min. 98 %, ACS, Alfa Aesar), acetone (99 % w/w, VWR Chemicals) were used as received. In flow cell tests, a vanadium 1.6 M electrolyte from Oxkem (Oxkem Limited (Reading, United Kingdom), was employed. Ultrapure water (resistivity ≥ 18.2 MΩ cm) was used to prepare working solutions.

3.2. Electrode Preparation and Surface Treatments

3.2.1. Felt Electrode Preparation

Prior to thermal treatments, the carbon felt samples were cleaned in acetone in ultrasonic cleaner, to remove eventual organic residues and other loose surface fibers and dried at 80 °C in oven until all moisture was removed.

3.2.2. Thermal Treatment of Electrodes

Thermal oxidation was performed in a furnace (Skutfire box) with a flow of reconstituted air. Heating was performed at a rate of 2 °C min^{-1}. After reaching the target temperature, samples were kept in the furnace for the specified dwell time. The furnace was left to cool down on its own. As a first pass study, the target temperatures were set at 400, 450, 500, and 600 °C. Dwell time was set at 0.5, 3, 6, and 12 hours for the selected temperatures. To evaluate the effect of increasing the total treatment time on surface functionalization, a double thermal treatment was conducted. This consisted of two consecutive 12-hour treatments at 450 °C. The various thermal treatment conditions were arranged as a full matrix and are provided in Table 1.

Table 1: Thermal treatment matrix: temperature and dwell time combinations tested

Temperature (°C)	0.5 h	3 h	6 h	12 h	12 h+12 h
400	✓	✓	✓	✓	×
450	✓	✓	✓	✓	✓
500	✓	✓	✓	✓	×
600	✓	✓	✓	✓	×

3.2.3. Chemical Treatment

Chemical treatment was performed in a 1 M sulfuric acid at 80 °C for a fixed treatment duration of 3, 7, 12, and 18 hours. The felt was removed from the acid and repeatedly rinsed with ultrapure water. The samples were dried in an 80 °C oven until all moisture was removed.

3.2.4. Combined and Sequential Treatments

The complete set of varied conditions tested is described in Table 2, including the treatment conditions introduced in the following subsections.

Table 2: Summary of combined and sequential surface treatment conditions

Condition	Sequence
Acid-first (screening)	1 M H_2SO_4 (3, 7, 12 or 18 h) → 450 °C, 12 h
Acid-first (temperature)	1 M H_2SO_4 (12 h) → 400 °C or 450 °C, 12 h
Alternating Thermal–Chemical Sequence	450 ºC, 6 h → 1 M H_2SO_4, 12 h → 450 °C, 6 h
Plasma (post-thermal)	450 °C, 12 h → N_2 plasma, 3 or 10 min
Propylene stabilisation	1 M H_2SO_4, 12 h → 450 °C, 12 h → C_3H_6 , 72 h
Bismuth electrodeposition	1 M H_2SO_4, 12 h → 450 °C, 12 h → Bi electrodeposition (negative electrode only)

3.2.5. Plasma Treatment

Plasma treatment was realized in a flow of N_2, in a plasma system (Plasma Lab system Zepto from Diener Electronic, Germany). The exposure time was 3 and 10 min. The treatment was applied to samples that previously underwent thermal oxidation at 450 °C for 12 h.

3.2.6. Bismuth Electrodeposition

Only the negative electrode felt was subjected to bismuth modification in order to improve the sluggish kinetics of the V^{2+}/V^{3+} redox couple, which is the rate-determining step in the operation of a VRFB [33].

Bismuth electrodeposition was performed ex-situ in a customary three-electrode half-cell. Treated carbon felt served as the working electrode, and a carbon rod and $Ag|AgCl|KCl_{sat}$ electrode (0.197 V *vs.* SHE) served, respectively, as the counter and reference. The deposition solution contained 0.05 M $Bi(NO_3)_3 * 5H_2O$ in 0.5 M HNO_3.

The felt was galvanostatically deposited of 2.5 mA (cathodic) for 3600 s, with a cathodic potential cut-off of −0.50 V *vs* Ag|AgCl. The felt was then rinsed with ultrapure water and dried at 80 °C.

3.2.7. Post-Treatment Stabilization in Propylene Atmosphere

After acid and thermal treatment, some felts were allowed to cool to room temperature before being transferred to a sealed borosilicate glass bottle fitted with a two-port cap. Propylene gas was introduced through one port while the second port remained open, allowing the incoming gas to displace the ambient atmosphere within the vessel. After an appropriate purge period, the gas feed was disconnected and both ports were sealed, establishing a static propylene atmosphere around the felt for the remainder of the storage period.

Felts were held under this static propylene atmosphere at room temperature for 72 h prior to cell assembly, with no intermediate purge or rinsing step between propylene storage and electrochemical testing.

3.3. Experimental Setup

3.3.1. Single-Cell Configuration

A custom-made single flow cell employed for the electrochemical tests. The main components of the cell are following: two carbon felt electrodes with a geometrical active area of 4 cm^2, separated by a membrane, two composite graphite plates and two gold plated copper plates. PTFE gaskets with total thickness of 3.5 mm were used to set the electrode compression to approximately 25 %. Viton gaskets were used to seal the cell and prevent leakage of the electrolyte. Figure 2 shows a photo of the assembled laboratory cell. The upscaling tests were conducted in a commercial Pinflow cell (Czech Republic) with carbon felt electrodes with a geometrical active area of 20 cm^2.

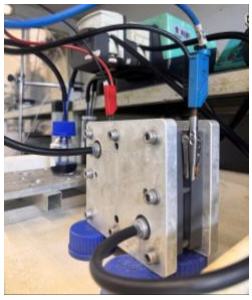


Figure 2: Image of the assembled single flow cell employed in the work.

3.3.2. Electrolyte Circulation System

The vanadium electrolyte was pumped through each half-cell by a Watson Marlow 323 peristaltic pump, set to a flow at the equivalent of 16 mL min^{-1}. One dual-channel pump unit was used to independently flow each half-cell. For the entire flow circuit, Tygon A-60-G tubing was selected for its chemical resistance to concentrated sulfuric acid and vanadium species. Each half-cell was connected to an electrolyte reservoir.

3.3.3. Measurement and Control Equipment

Electrochemical measurements were performed with a Zahner Zennium potentiostat, using a Zahner PP242 power potentiostat booster (±5 V, ±40 A) when relevant, with the Thales XT software.

3.4. Electrochemical Testing Procedures

3.4.1. Electrical Conductivity Measurements

To measure the through-plane electrical conductivity of carbon felt electrodes, a Conductivity Meter Press CMP-5 (Vasco da Gama CoLAB; Porto, Portugal; serial no. 2025-002) was used. The measurement setup used consisted of two (2) graphite plates and two (2) carbon felt samples constructed to simulate the layer design of a battery cell. Measure Press CMP-5 reported the through-plane electrical resistance of the sample stack using a direct DC current of 315 mA.

According to DIN EN ISO 5084 (Determination of thickness of textiles and textile products), the felt thickness was ascertained by applying a pressure of 1.0 kPa, the benchmark cited by the felt supplier. The sample used was 5 cm x 5 cm and corresponded to a contact area of 25 cm^2. A normal load of 2.5 N was applied to achieve the stated pressure. This measure was standard and left no ambiguity about the thickness of the felt in the conductivity calculations and the stated nominal thickness by the manufacturer.

In the Custom Distance test mode, the range of compression was defined in relation to the thickness measured. Before the measurements, the total thickness of the four-layer stack was measured, including the thickness of the two graphite current-collecting plates. A range of 0-30 % compression was applied. The measured values of resistance and conductivity (Ω and Ω^{-1} mm^{-1}, respectively) were saved in the CSV file.

3.4.2. Cyclic Voltammetry

For the cyclic voltammetry (CV) studies, a three-electrode half-cell assembly was used. The working electrode, carbon felt, was paired with a carbon rod counter electrode and an $Ag|AgCl|KCl_{sat}$ electrode (0.197 V *vs.* SHE).

All CV studies were conducted in a commercial 1.6 M Vanadium electrolyte diluted 4 times with a 2 M H_2SO_4. A total of three CV cycles were recorded per experimental condition. The first cycle was discarded as the initial sweep typically shows a different shape. The second cycle was therefore taken as representative.

To derive current densities, the geometric area of the felt electrode was considered.

Peak-to-peak separation was determined from the corrected anodic and cathodic peaks as:

$$\Delta E_p = E_{p,a} - E_{p,c} \tag{8}$$

The peak current ratio, which also served as a measure of reaction reversibility in combination with ΔEp was determined from:

$$r = \left|\frac{i_{p,a}}{i_{p,c}}\right| \tag{9}$$

The calculation procedures made with a custom Python program can be found in the Appendix F - Python-Based Data Processing Scripts.

3.4.3. Electrochemical Impedance Spectroscopy and Polarisation Measurements

Prior to the impedance measurement, the vanadium flow cell was charged to approximately 50 % state of charge at a constant voltage of 1.4 V. EIS was then performed at open-circuit potential (OCP) on the charged cell over a frequency range of 100 kHz to 50 mHz with a signal amplitude of 5 mV. Data were collected by taking 10 readings per decade above 66 Hz and 5 readings at lower frequencies. The ohmic resistance (R_s) and the charge transfer resistance (R_{ct}) were determined geometrically from the Nyquist plots: R_s was taken as the high-frequency intercept of the spectrum with the real axis, and R_{ct} as the diameter of the semicircle [12].

After the impedance test, polarization measurements were performed under the same charging conditions described, with the scan rate 10 mV s^{-1} until a potential difference of 0 V was reached.

Calculation for polarization were done using a custom-made Python program. The methods used for calculations and computing methods can be found in Appendix F.

3.4.4. Charge–Discharge Cycling

The cycling was performed with a constant current with the cut off potential differences set at 1.6 V and 0.8 V. During the performance characterization of the treatment conditions, the primary screening current density was set to 150 mA cm^{-2}.

Cycling performance was assessed through the coulombic (CE), voltage (VE), and energy efficiencies (EE). Coulombic efficiency measures the amount of charge that is regained during

discharge of the system, relative to the amount of charge that is supplied during the charging step of the cycle and it is calculated using equation:

$$\mathrm{CE} = \frac{Q_{\mathrm{disch}}}{Q_{\mathrm{charge}}} = \frac{\int I_{\mathrm{disch}}, dt}{\int I_{\mathrm{charge}}, dt} \quad (10)$$

Voltage Efficiency (VE) is defined as the ratio between discharge and charge voltages over a cycle, and is calculated using the following equation:

$$\mathrm{VE} = \frac{\bar{V}\mathrm{disch}}{\bar{V}\mathrm{charge}} \quad (11)$$

Energy Efficiency (EE) is defined as the product of coulombic and voltage efficiencies, and is a measure of the round-trip efficiency of the system:

$$\mathrm{EE} = \mathrm{CE} \times \mathrm{VE} = \frac{E_{\mathrm{disch}}}{E_{\mathrm{charge}}} = \frac{\int V_{\mathrm{disch}} \cdot I, dt}{\int V_{\mathrm{charge}} \cdot I, dt} \quad (12)$$

The metrics of the 3rd charge-discharge cycle were used for comparison. For comparison across a selected number of cycles, Appendix E presents mean CE, VE and EE for all conditions evaluated in this work.

The computational procedure by way of a python custom made program used to obtain these quantities from the recorded voltage–current–time data is detailed in Appendix F -Python-Based Data Processing Scripts.

3.4.5. Scanning electron microscopy with energy-dispersive X-ray spectroscopy (SEM-EDS)

Surface morphology of the carbon felt electrodes was examined before and after the different treatments using a Phenom XL scanning electron microscope equipped with an energy-dispersive X-ray spectroscopy (EDS) detector. Micrographs allowed direct comparison of fiber surface texture and structural changes for untreated and treated felts.

4. Results and discussion

4.1. Effect of thermal treatment (temperature and duration, combined)

The first stage of treatment optimization aimed to identify the thermal oxidation conditions that maximized energy efficiency (EE) at 150 mA cm^{-2}. Measurement of the conductivity of compressed felt electrodes before electrochemical tests is a preliminary screening tool; cyclic voltammetry of felt electrodes gives insight into effect of treatment on the electrochemical activity of electrodes in electrolytes towards V(II)/V(III) redox pairs, and battery cycling allows to identify the effect of treatment parameters on coulombic, voltaic and energy efficiencies.

4.1.1. Electrical conductivity

The through-plane electrical conductivity was measured for stacked samples (2 felts and 2 graphite bipolar plates) under increasing compression.

The results are presented in Figure 3.

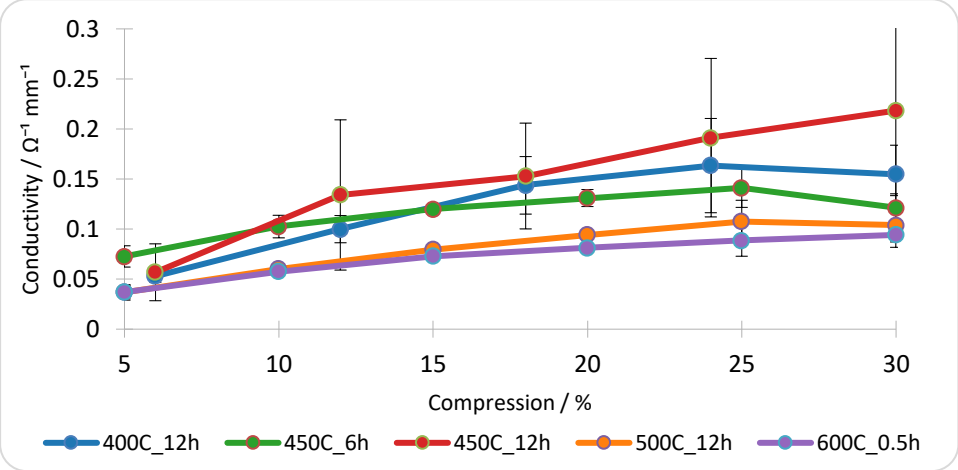


Figure 3: Effect of compression level of felt samples on the electric conductivity.

As expected, the felt conductivity increased with compression level. The as-received carbon felt material has a porosity about 94 %, according to the supplier specifications. As the porous felt is compressed, there is a reduction in inter-fiber voids. Consequently, there is an increase in contact area between the fibers and between the fibers and the current collector, which in turn reduces the through-plane resistance.

It can be seen that the felt's electrical conductivity decreases as the temperature of treatment increases. The higher-temperature treatments presumably are more aggressive towards the fiber structure, and can promote more intensive surface oxidation of the fibers, reducing thus the mechanical strength, disrupting conductive pathways, and eventually increasing electrical resistance [20].

The stack with samples treated at 450 °C/12 h exhibited the highest mean conductivity, but also higher variability, as the standard deviation at higher compression (24 % and 30 %) was almost equal to the mean of the sample. This variability should be considered when evaluating this preliminary result. The 450 °C/12 h sample was potentially the most favorable sample based on this preliminary screening.

4.1.2. EIS Results

EIS measurements were conducted at open-circuit potential around 50 % state of charge. The Nyquist spectra are shown in Figure 4.

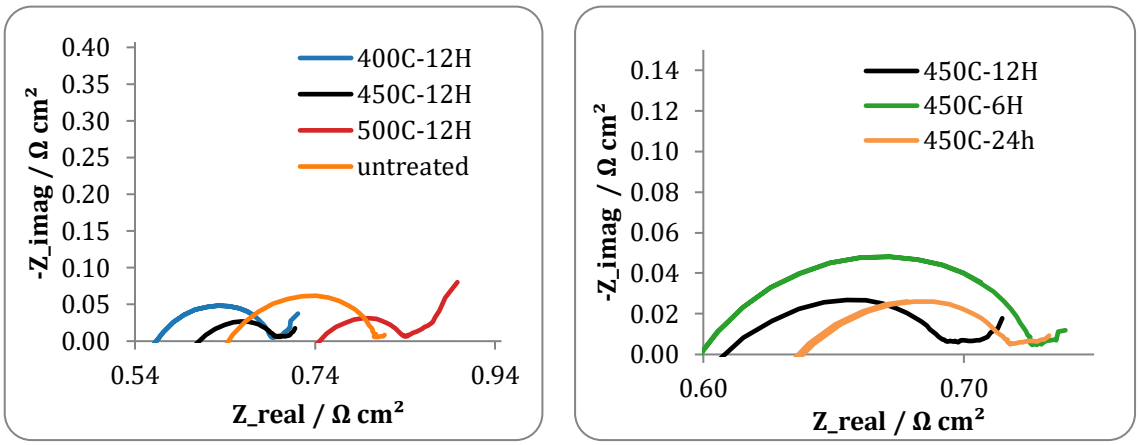


Figure 4: Nyquist plots obtained for the flow cell assembled with felt electrodes treated at different conditions (a) (left) Temperature series (untreated, 400 °C, 450 °C, and 500 °C, all at 12 h). (b) (right) Duration series at 450 °C (6, 12, and 24 h).

The parameters R_s and R_{ct}, are summarized in Table 3.

Table 3: EIS-derived ohmic and charge-transfer resistance across the thermal screening matrix

Sample	R_s **(Ω cm²)**	R_{ct} **(Ω cm²)**
Untreated	0.646	0.165
400 °C-12 h	0.558	0.134
450 °C-6 h	0.597	0.131
450 °C-12 h	0.615	0.081
450 °C-12 h+12 h	0.631	0.088
500 °C-3 h	0.600	0.141
500 °C-12 h	0.74	0.095

The highest R_s are found for the cells assembled with untreated felt electrodes and treated at 500 °C for 12 h. Except for the latter, thermal treatment of felt electrodes allows for

decreasing the R_s of the cell. As shown in Table 3, in the series of treated samples, in general, as the temperature of treatment increases, the R_s tends to increase, with the exception of the sample 500 ºC/3 h.

The EIS response of samples treated at 450 ºC shows an increase in R_s with treatment duration: from 0.597 Ω cm² for 6 h treatment to 0.631 Ω cm² for the total 24 h treatment, although all being below the R_s of the cell with the untreated sample (0.646 Ω cm²).

All thermal treatments performed resulted in a decrease of R_{ct} in comparison with the nontreated one. At 450 ºC, the 12 h treatment yielded the lowest R_{ct} in the series, 0.081 Ω cm², while the double 12 h treatment resulted in a slight increase of R_{ct} to 0.088 Ω cm². The effect of treatment duration on R_s and R_{ct} at 450 ºC in this work is different from the data reported in [19] where the 8-24 h treatment at 400 ºC for the same type of felt material was explored, and the duration had a positive effect on both R_s and R_{ct}, decreasing these parameters.

4.1.3. Battery cycling performance

The performance metrics of flow cells assembled with different felt electrodes and tested at a current density of 150 mA cm^{-2} are summarized in Table 4.

Table 4: Cycling performance across the thermal screening matrix (150 mA cm^{-2}, reference cycle)

Sample	**CE (%)**	**VE (%)**	**EE (%)**
Untreated	85.28	80.51	68.65
400°C–12 h	95.99	82.09	78.81
450°C–6 h	83.27	78.92	65.73
450°C–12 h	95.92	83.49	**80.09**
500°C–3 h	83.72	81.77	68.45
500°C–12 h	96.40	68.67	66.21
600°C–0.5 h	95.69	80.16	76.70

The highest EE of 80.09 % was achieved in the cell with electrodes treated at 450 °C for 12 h. At 400 °C, EE remained slightly lower (78.81 %) despite a comparable CE (95.99 %). At 500 °C, the picture changes substantially: CE remains high at the 12-hour dwell (96.40 %), but VE drops sharply to 68.67 %, putting EE down to 66.21 %. This pattern, high CE paired with a collapsing VE, is consistent with progressive loss of electrical conductivity and mechanical integrity of the carbon fibers at elevated temperature, which increases internal resistance,

consistent with the conductivity measurements presented earlier. At 600 °C, the very short 0.5-hour dwell still gave a reasonably high EE of 76.70 %, due to the decent CE (95.69 %).

Treatment duration also influenced cell metrics. At 450 °C, and at 500 ºC, longer dwell is beneficial for CE. At 450 ºC, 6-hour dwell gave a markedly lower EE (65.73 %) than the 12-hour dwell (80.09 %), despite identical temperature, indicating probably that 6 hours is insufficient to functionalize the felt to the same extent at this temperature. The 500 °C, 3 hour condition gave the lowest CE of any thermal-only sample on the reference cycle (83.72 %), suggesting this short, hot treatment may have produced a felt that was inconsistently activated, structurally compromised, or both. Prolonged treatment, 12 h, although resulted in higher CE, which is consistent with smaller R_{ct}, but yielded lower VE, due to increased R_s, as seen in Table 4, and brought a lower EE, when compared to the sample treated at 500 ºC for shorter time (3 h).

A double thermal treatment (450 °C for 12 hours, repeated twice consecutively) was also tested, to assess whether extending total oxidation time would yield further improvement. This gave a reference-cycle EE of 78.72 %, essentially indistinguishable from the single 12-hour treatment and slightly below it, suggesting that a second thermal pass does not provide additional benefit.

On this basis, 450 °C for 12 hours was selected as the optimal thermal treatment condition and was carried forward as the thermal step paired with chemical (acid) pre-treatment in the combined treatment sequence discussed in Section 4.2.

4.2. Chemical pre-treatment (acid-first) combined with thermal

4.2.1. CV analysis

Cyclic voltammetry was conducted on the acid-first treated felts using a three-electrode half-cell set-up. For the purposes of this study, the second cycle was considered representative, as the further cycles resembled the second one for all samples. The performance of felt electrodes towards the V^{2+}/V^{3+} redox couple representing the redox processes at the negative electrode was analyzed. The recorded cyclic voltammetry curves are given on Figure 5. The main parameters, such as peak separation (ΔEp), the peak current ratio (ipa/ipc) for the V^{2+}/V^{3+} couple are provided in Table 5, and discussed here in detail, as this redox reaction is considered rate determining [15], [24].

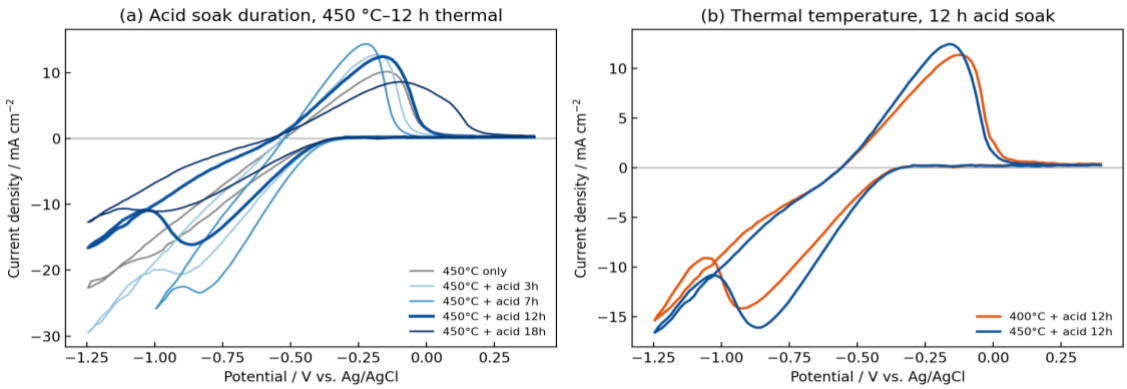


Figure 5: Cyclic voltammograms recorded at felt electrodes in the electrolyte containing V^{2+}/V^{3+} redox pair: (a) felt electrodes differing in duration of acid pretreatment step - no pretreatment, 3, 7, 12 and 18 h, (b) felt electrodes treated in acid for 12 h, and further at 400 ºC or 450 ºC for 12 h.

Table 5: CV peak separation and peak current ratio for the V^{2+}/V^{3+} couple, acid-first treatments

Sample	ΔEp **(mV)**	**ipa/ipc**
450 ºC only (baseline)	875	0.567
450 ºC + acid 3 h	677	0.643
450 ºC + acid 7 h	594	0.626
450 ºC + acid 12 h	726	0.765
450 ºC + acid 18 h	858	0.780
400 ºC + acid 12 h	809	0.799

As Figure 5 presents, the 450 °C-only baseline (without acid) produces the least resolved, most broad voltammogram in the series. This behavior is consistent with the high ΔEp and low peak current ratio reported in Table 5. For the 7h treatment, the resolution of both peaks significantly improves, and the ΔEp narrows to the lowest in the series. The voltammograms for the 12h and 18h treatments show broader peaks and a higher ΔEp parameter, although the peak current ratio becomes close to 1 in comparison with other voltammograms.

A clear increasing trend is observed in the peak current ratio with increasing acidic treatment duration, from 0.643 for the 3 h treatment to 0.780 for the 18 h treatment. As the peak current ratio approaching 1.0 it indicates an improvement in the reversibility of the V^{2+}/V^{3+} reaction, the prolonged treatment is beneficial for improving electrode kinetics. One can conclude that acid pretreatment, from 3 h onward, improves electrode kinetics compared to solely thermal treatment. The subsequent thermal treatment, whether at 400 or 450 °C, with the same duration, 12 h, results in the comparable performance.

4.2.2. EIS Results

The Nyquist spectra of the cells assembled with felt electrodes subjected to acidic pretreatment are shown in Figure 6. R_s and R_{ct} are given in Table 6.

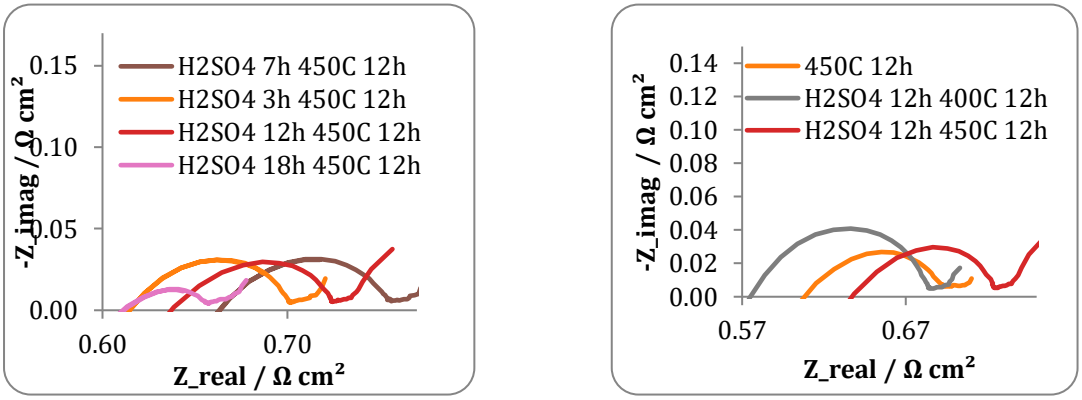


Figure 6: Nyquist plots for felt electrodes after different treatments: (a) acidic treatment duration (3, 7, 12, 18 h), (b) 12 h acid + thermal at 400/450 °C vs. thermal-only at 450 °C.

Table 6: EIS-derived ohmic and charge-transfer resistance for acid-first treatments

Sample	R_s **(Ω cm²)**	R_{ct} **(Ω cm²)**
450 °C-12 h (thermal only)	0.615	0.081
450 °C-12 h + H_2SO_4 3 h	0.613	0.088
450 °C-12 h + H_2SO_4 7 h	0.658	0.1
450 °C-12 h + H_2SO_4 12 h	0.64	0.084
450 °C-12 h + H_2SO_4 18 h	0.604	0.054
400 °C-12 h + H_2SO_4 12 h	0.575	0.109

For the thermal-only baseline, R_{ct} is 0.081 Ω cm²; with the introduction of acid treatment, R_{ct} becomes smaller, from the 12 h duration onwards. This aligns with the acid treatment addressing the internal pore structure of the felt fabric before proceeding to thermal oxidation, which permits the thermal step to activate a greater portion of the felt fabric surface. Within the tested range, the best R_{ct} (0.054 Ω cm²) results from acidic pretreatment of 18 hours.

R_s, in contrast to R_{ct}, showed a different pattern, particularly a non-monotonic one. From a baseline of 0.615 Ω cm² for the thermal only sample, R_s decreased at 3 h and 18 h.

The 400 °C/12 h treatment with a 12 h acid treatment displays underperforming behavior compared to the 450 °C treatment. R_{ct}, is twice the values found for acid treatment at 450 °C. Even so, R_s is lower than all acid treatment conditions at 450 °C. This implies that the acid

treatment's influence on charge-transfer resistance is not significantly reliant on the temperature of the thermal treatment, at least for the 400 °C and 450 °C treatments.

4.2.3. Polarization Results

The polarization metrics for the cells with the felt electrodes prepared by acidic and subsequent thermal treatment are presented in Table 7, with the relevant current and power density curves shown in Figure 7.

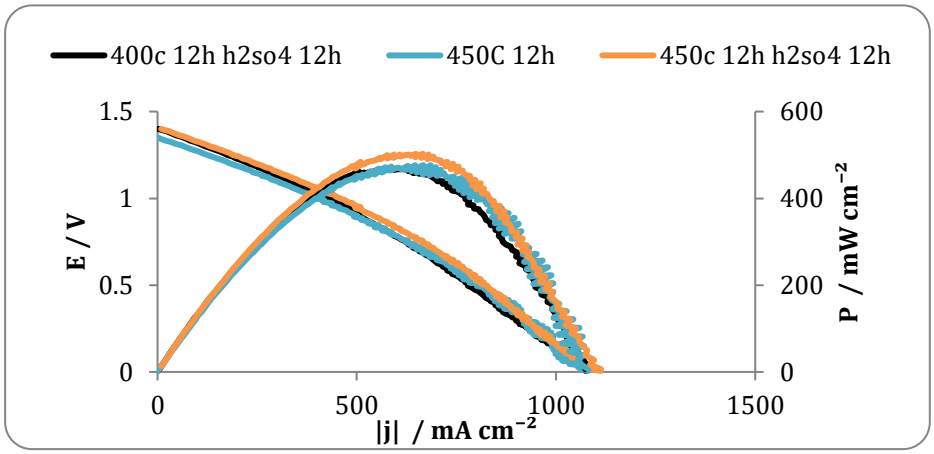


Figure 7: Polarization and power-density curves for acid-first treatments across acid-soak durations and thermal-step temperature

Table 7: Polarisation metrics for acid-first treatments

Sample	Max Pd (mW cm^{-2})	Limiting j (mA cm^{-2})
450 °C-12 h (thermal-only)	476.7	1081.3
450 °C-12 h, H2SO4-3 h	462.7	1007
450 °C-12 h, H_2SO_4-7 h	479.6	1117.3
450 °C-12 h, H_2SO_4-12 h	502.6	1112.9
450 °C-12 h, H_2SO_4-18h	537.9	1223.7
400 °C-12 h, H_2SO_4-12 h	469.4	1075.8

Longer acidic pretreatment is beneficial for maximum power density: peak power density at 3 h was 462.7 mW cm^{-2}, increased to values of 479.6 mW cm^{-2} at 7 h, 502.6 mW cm^{-2} at 12 h, and 537.9 mW cm^{-2} at 18 h. All the acid treatment conditions over 3 hours performed better than the 450 °C-only baseline of 476.7 mW cm^{-2}.

The limiting current density exhibited a non-monotonic behavior. The treatment time of 18 h resulted in the highest limiting current density of all the acid-first conditions, reaching 1223.7 mA cm^{-2}. The 7 h and 12 h treatment resulted in limiting current densities of 1117.3 and 1112.9 mA cm^{-2}, respectively.

4.2.4. Battery cycling performance

The performance metrics of the cells assembled with felt electrode subjected to acidic pretreatment and tested at a current density of 150 mA cm^{-2} are given in Table 8.

Table 8: Cycling performance of cells with felt electrodes treated at different acid-soak durations prior to 450 °C–12 h thermal treatment (150 mA cm^{-2}, reference cycle)

Sample	**CE (%)**	**VE (%)**	**EE (%)**
450°C–12 h (thermal-only)	95.92	83.49	80.09
450°C–12 h, H_2SO_4–3 h	98.04	81.50	79.90
450°C–12 h, H_2SO_4–7 h	98.38	81.85	80.53
450°C–12 h, H_2SO_4–12 h	99.11	83.26	82.52
450°C–12 h, H_2SO_4–18h	95.62	83.70	80.03

Coulombic efficiency improved with treatment time, reaching a peak of 99.11 % after a 12 h treatment, and then dropped to 95.62 % after an 18 h treatment. The voltage efficiency remained between 81.50 and 83.70 % and also benefits from the acidic pretreatment duration. As a result, Energy efficiency improved with acid treatment time, reaching the highest value of 82.52 % after a 12 h treatment (compared to 80.09 % for the thermal-only baseline) before declining at 18 h.

The effect of acidic pretreatment duration on CE can be ascribed to the effective etching and progressively opening the felt's internal pore structure, which, in turn, exposed more fiber surfaces to the subsequent thermal functionalization. As a result, the CE achieves its maximum. Prolonged acidic treatment, although beneficial for decreasing R_S and improving VE, along with subsequent thermal treatment, resulting in decreased reversibility of redox reactions on the felt surface, as shown in the CV data in Table 5, and a decrease in CE.

SEM micrographs of the untreated, thermal-only, and acid-first treated felts are provided in Appendix D, though no significant morphological differences were identified between the treatments.

A 12 h thermal treatment at 400 °C showed the lowest measured R_S in comparison to the 450 °C thermal treatment. Therefore, the acid first sequence was carried out at 400 °C, with a 12 h treatment, to establish if a lower thermal treatment temperature than 450 °C with the acid treatment would achieve better results. The performance metrics of flow cells with the electrodes differing by the temperature of treatment following acidic treatments shown in Table 9.

Table 9: Cycling performance of acid-first treatment (H_2SO_4, 12 h) at 400 °C vs. 450 °C thermal step (150 mA cm^{-2}, reference cycle)

Sample	**CE (%)**	**VE (%)**	**EE (%)**
H_2SO_4–12 h, 400°C–12 h	98.38	82.07	80.74
H_2SO_4–12 h, 450°C–12 h	99.11	83.26	82.52

The felt electrodes treated at higher temperature showed slightly higher CE and VE, and consequently, better EE values: energy efficiency was at 80.74 % at 400 °C and 82.52 % at 450 °C. Based on these, one can still apply 450 °C as the preferred thermal treatment parameter for the acid-first sequence.

4.2.5. Alternating Thermal-Chemical Sequence (Thermal–Acid–Thermal)

An alternative sequence of acidic and thermal treatments was explored. Here, the 12-hour thermal treatment was split into two thermal treatments of 6 hours each, at 450 °C, with the acid treatment (H_2SO_4, 12 h) placed in between. Instead of relying on the acid treatment to expand the felt fiber structure, this method used thermal treatment to introduce the first step in the sequence prior to the acid treatment. This method was compared to the acid-first method (H_2SO_4–12 h, 450°C–12 h, EE 82.52 % at the reference cycle).

Cycling performance was inferior to the acid-first method for all three efficiency metrics. The alternating method achieved a reference cycle CE, VE, and EE of 94.59 %, 82.67 %, and 78.20 %, respectively; the acid-first method achieved a CE of 99.11 %, a VE of 83.26 %, and an EE of 82.52 %. While voltage efficiencies of both methods were similar, the alternating method resulted in a lower coulombic efficiency, indicating the presence of extensive side reactions or insufficient felt activation.

EIS measurements showed the alternating treatment had a R_{ct} of 0.144 Ω cm^2, compared to 0.084 Ω cm^2 for acid first; the treatment R_s was comparable (0.59 Ω cm^2 *vs* 0.64 Ω cm^2). The alternating treatment brought an R_{ct}, approximately twice that of the acid-first treatment, and with comparably consistent R_s, showed less effective electrocatalytic activation of the electrodes, consistent with the lower coulombic efficiency seen in cycling.

Polarization data were also inconclusive in identifying the two sequences. The method produced a higher peak power density of 515.2 mW cm^{-2} at 0.755 V compared to 502.6 mW cm^{-2} in the acid-first case, and a higher limiting current density of 1164.2 mA cm^{-2} as opposed to 1112.9 mA cm^{-2} .

Overall, the alternating thermal–chemical sequence was not superior to the acid-first sequence regarding the most important metric for cell operation: energy efficiency. This remained the case even as the alternating thermal–chemical sequence demonstrated some

advantages in raw power and limiting-current capabilities. A lower coulombic efficiency shows that the insertion of a thermal dose before and after the acid step is less efficient at functionalizing the felt than the application of an acid treatment, followed by the full thermal treatment. This result, therefore, supports the acid-first mechanism proposed in Section 4.2. The acid-first sequence (H_2SO_4–12 h, 450 °C–12 h) was therefore retained as the leading treatment condition going into the remaining sections of this chapter.

4.3. Plasma treatment

Plasma treatment was explored as a potential enhancement on top of a leading treatment condition described in Section 4.2. The acid-first condition served as a benchmark. A nitrogen atmosphere was chosen for the plasma discharge because of the ability of nitrogen plasma to introduce a variety of nitrogenous functional groups (*e. g.* C–N and C=N) as opposed to the oxygen-containing functional groups produced by thermal oxidation, which may provide additional active sites for vanadium redox reactions.

4.3.1. EIS Results

EIS was conducted for both durations of plasma treatment. The Nyquist plots are overlaid in Figure 8 with the acid-first baseline for comparison. The results for R_s and R_{ct} are presented in Table 10.

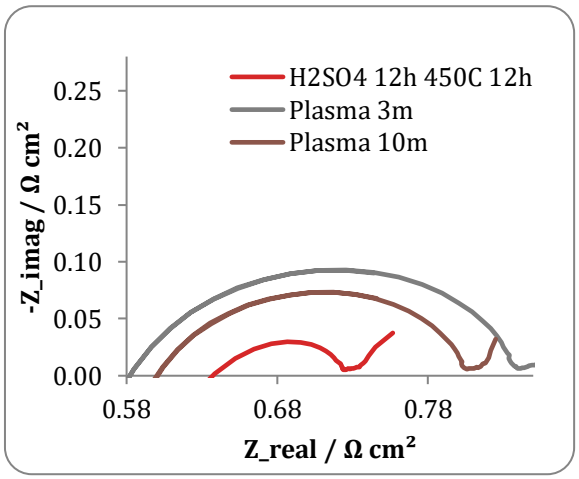


Figure 8: Nyquist plots recorded for flow cells assembled with felt electrodes subjected to different activation procedures: baseline acid treatment followed by thermal activation, and additional N_2 plasma treatment for different durations.

Table 10: EIS-derived ohmic and charge-transfer resistance for plasma-treated electrodes vs. acid-first baseline

Sample	R_S (Ω cm²)	R_{ct} (Ω cm²)
450 °C-12 h + H_2SO_4 12 h (acid-first baseline)	0.64	0.084
450 °C-12 h + H_2SO_4 12 h + N_2 plasma 10 min	0.604	0.204
450 °C-12 h + H_2SO_4 12 h + N_2 plasma 3 min	0.585	0.257

Compared to the acid-first baseline, plasma treatment increased R_{ct} in both exposure cases. After 10 minutes of exposure, the R_S showed a slight decrease due to plasma treatment. This might indicate that the treatment did not degrade the bulk electrical contact of the felt and may have improved the contact, despite its adverse effect on charge-transfer kinetics at the electrode.

The 3-minute exposure produced a higher R_{ct} than the 10-minute exposure. This result is non-monotonic with respect to exposure time. It is likely that both plasma exposures are physically etching or roughening the felt surface with no improvement in charge-transfer kinetics at the negative electrode.

4.3.2. Polarization results

The polarization results are given in Table 11, with the associated power density curves in Figure 9, along with the acid-first baseline.

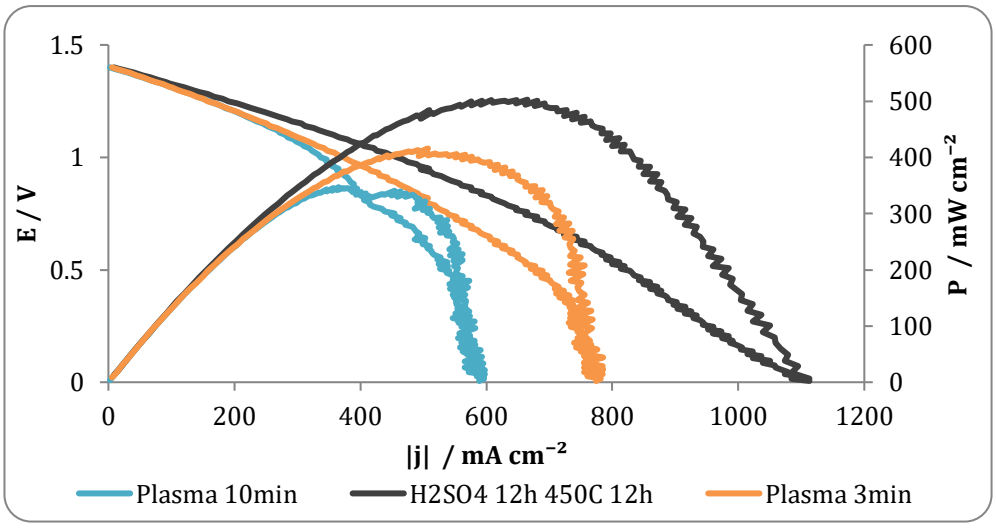


Figure 9: Polarization and Power Density curves recorded for single cells assembled with felt electrodes subjected to different treatment procedures, the conditions are indicated on the plot

Table 11: Polarization metrics for plasma-treated electrodes vs. acid-first baseline

Sample	**Max Pd (mW cm⁻²)**	**Limiting *j* (mA cm⁻²)**
450 ºC-12 h + H2SO4 12 h (acid-first baseline)	502.6	1112.9
450 ºC-12 h + H2SO4 12 h + N_2 plasma 10 min	346.9	597.7
450 ºC-12 h + H2SO4 12 h + N_2 plasma 3 min	415.8	785.4

Peak power density exhibited baseline acid-first treatment values over the ones recorded for plasma treatment combined with acid treatment at both exposure times.

For limiting current density, a similar trend as peak power density was observed for the 3 minute condition with a decrease from limiting current density baseline of 1112.9 mA cm^{-2} to 785.4 mA cm^{-2}.

Similar to R_{ct}, for the 3-minute exposure, polarisation metrics were closer to the acid-first baseline compared to the 10-minute exposure. For the 10-minute exposure, peak power density was lower than the 3-minute exposure (346.9 *vs.* 415.8 mW cm^{-2}).

4.3.3. Battery cycling performance

Battery cycling performance was evaluated at 150 mA cm^{-2} for both exposures. Reference-cycle efficiency values shown in Table 12.

Table 12: Cycling performance for plasma-treated electrodes *vs.* acid-first baseline (150 mA cm^{-2}, reference cycle)

Sample	**CE (%)**	**VE (%)**	**EE (%)**
450 ºC-12 h + H_2SO_4 12 h (acid-first baseline)	99.11	83.26	82.52
450 ºC-12 h + H_2SO_4 12 h + N_2 plasma 10 min	97.13	78.33	76.09
450 ºC-12 h + H_2SO_4 12 h + N_2 plasma 3 min	92.81	78.41	72.77

Comparing energy efficiency at the acid-first baseline, there was a decline in efficiency due to plasma treatment at both lengths of exposure. For the 10-minute exposure, the acid-first baseline value was at 82.52 %, compared to 76.09 %. For the 3-minute exposure, the value was at 72.77 %. Hence, there was a decrease of 6.4 and 9.8 percentage points, respectively.

Coulombic efficiency at the baseline was 99.11 % and decreased to 97.13 % and 92.81 % after 10 minutes and 3 minutes, respectively. Voltage efficiency decreased from 83.26 % to 78.33 % and 78.41 %, respectively. Both plasma conditions yielded nearly the same voltage efficiency, despite the differences in coulombic efficiency. It is therefore notable that the largest coulombic efficiency degradation is seen at 3 minutes, rather than 10 minutes. This is consistent with the non-monotonic behavior previously reported for R_{ct} and the polarisation

metrics, which showed that the 3-minute condition performed worse than the 10-minute condition. For the 10-minute exposure, the acid-first baseline value was at 82.52 %, compared to 76.09 %. For the 3-minute exposure, the value was at 72.77 %. Hence, there was a decrease of 6.4 and 9.8 percentage points, respectively. Therefore, both plasma exposure conditions rank below the acid-first baseline and the thermal-only baseline presented in (EE 80.09 %). Hence, the plasma treatment was not justified in whichever context it was compared to.

Neither condition, improved on the acid-first baseline on any metric, and no exposure time within the tested range (3–10 minutes) is recommended as a refinement to the acid-first treatment.

4.4. Post-Treatment Conditioning in Propylene Atmosphere

Felt samples underwent an acid-first treatment (H_2SO_4–12 h, 450 °C–12 h) then were left under a static propylene environment at room temperature for 72 h prior to cell assembly. The acid-first treatment (EE 82.52 % at reference cycle) was kept as the baseline for the comparisons in this section.

4.4.1. CV analysis

Cyclic voltammograms of the felt electrodes with and without propylene conditioning with response towards V^{2+}/V^{3} redox pair are given on Figure 10. The peak separation (ΔEp) and peak current ratio (*ipa*/*ipc*) for the system are shown in Table 13.

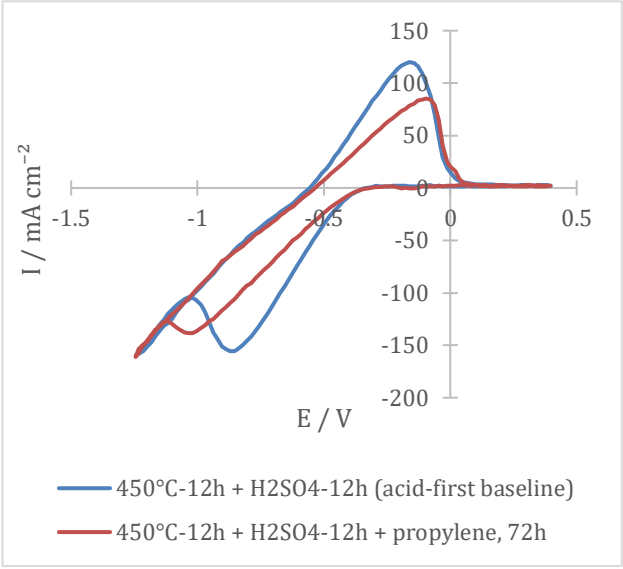


Figure 10: Cyclic voltammograms of the V^{2+}/V^{3+} couple recorded at felt electrodes after different treatment procedures: propylene conditioning vs. acid-first baseline

Table 13: CV peak separation and peak current ratio for the V^{2+}/V^{3+} couple at felt electrodes after different treatment procedures

Sample	ΔEp (mV)	ipa/ipc
450°C-12 h + H2SO4-12 h (acid-first baseline)	726	0.765
450°C-12 h + H2SO4-12 h + propylene, 72 h	920	0.624

The peak separation for the samples after propylene conditioning increased from 726 mV to 920 mV from the acid-first baseline, while the peak current ratio decreased from 0.765 to 0.624. These trends demonstrate a decrease in the reversibility of the V^{2+}/V^{3+} couple post-propylene exposure.

4.4.2. EIS Results

The Nyquist plots of both samples can be found in Figure 11. The acid-first baseline is included in Table 14 with the he R_s and R_{ct} values.

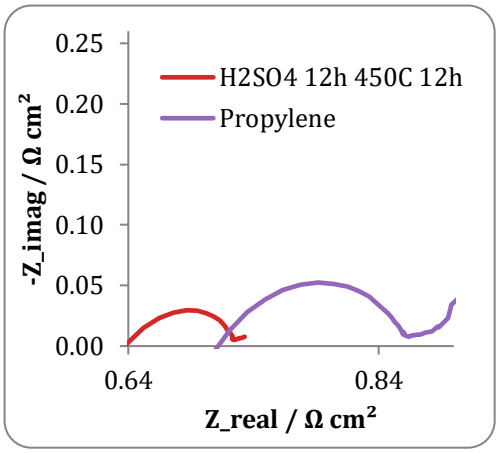


Figure 11: Nyquist plots for flow cells assembled with felt electrodes after different treatment procedures: propylene conditioning vs. acid-first baseline

Table 14: EIS-derived ohmic and charge-transfer resistance for propylene-conditioned electrodes vs. acid-first baseline

Sample	R_s (Ω cm²)	R_{ct} (Ω cm²)
450 °C-12 h + H_2SO_4-12 h (acid-first baseline)	0.64	0.084
450 °C-12 h + H_2SO_4-12 h + propylene, 72 h	0.717	0.144

Both R_s and R_{ct} increased following propylene conditioning: R_s increased slightly from 0.64 to 0.717 Ω cm² while R_{ct} increased from 0.084 to 0.144 Ω cm².

4.4.3. Polarization results

The polarization data can be found in Table 15. The power density and polarization curves can be found in Figure 12.

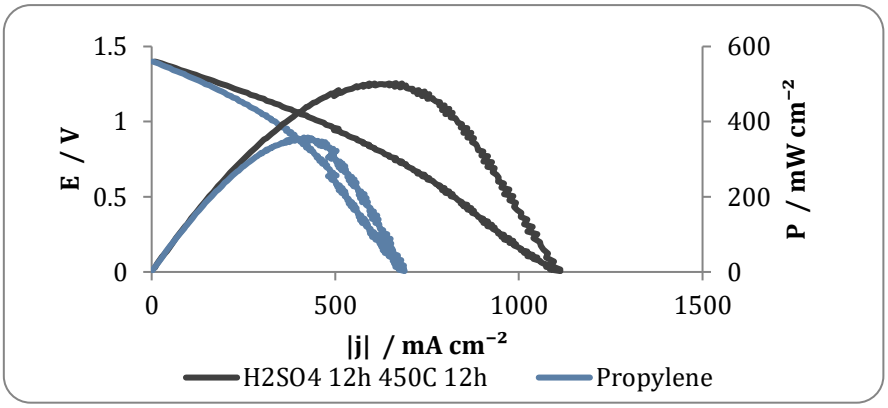


Figure 12: Polarization and power-density curves, propylene-conditioned electrodes vs. acid-first baseline

Table 15: Polarization metrics for propylene-conditioned electrodes vs. acid-first baseline

Sample	Max Pd (mW cm^{-2})	Limiting *j* (mA cm^{-2})
450°C-12 h + H2SO4-12 h (acid-first baseline)	502.6	1112.9
450°C-12 h + H2SO4-12 h + propylene, 72 h	357.8	688.5

After the propylene conditioning (after acid), peak power density showed a reduction from 502.6 mW cm^{-2} to 357.8 mW cm^{-2} and limiting current density also showed a decrease from 1112.9 mA cm^{-2} to 688.5 mA cm^{-2}.

4.4.4. Battery cycling performance

The reference-cycle efficiency values are listed in Table 16:

Table 16: Cycling performance for propylene-conditioned electrodes vs. acid-first baseline (150 mA cm^{-2}, reference cycle)

Sample	CE (%)	VE (%)	EE (%)
450 °C-12 h + H_2SO_4-12 h (acid-first baseline)	99.11	83.26	82.52
450 °C-12 h + H_2SO_4-12 h + propylene, 72 h	94.87	82.06	77.85

Energy efficiency at the acid-first baseline stands at 82.52 % declining to 77.85 % after propylene conditioning, a drop of 4.7 %. This was mainly due to a decline in coulombic efficiency from 99.11 % to 94.87 % (a drop of 4.2 %), while voltage efficiency was marginally impacted, declining from 83.26 % to 82.06 % (1.2 %). These results are consistent with the loss

of reversibility after propylene conditioning as shown by CV and increase of both R_s and R_{ct} evident from EIS data.

4.4.5. Discussion

Across all three measurement types, propylene conditioning underperformed the acid-first baseline: R_{ct} increased, peak separation widened and reversibility declined. Peak power density and limiting current density all worsened, carrying through to a 4.7-percentage-point reduction in energy efficiency by cycling. As with plasma treatment, propylene conditioning as applied here did not improve on the leading acid-first treatment condition, and the cycling efficiency changes was qualitatively similar between the two post-treatment steps, suggesting a shared mechanism: neither plasma exposure nor propylene conditioning adds further electrocatalytic activation beyond the acid-first sequence, and both instead measurably degrade it. The acid-first sequence (H_2SO_4–12 h, 450 °C–12 h) is therefore retained as the leading treatment condition going into the remaining sections of this chapter.

4.5. Bismuth electrodeposition

4.5.1. CV analysis

As with the other treatment conditions, primary attention was given to the V^{2+}/V^{3+} couple at the negative electrode, since this is the couple that the bismuth deposit selectively targets [33], the positive electrode was left at the baseline acid–thermal treatment only. The CV of the Bi-modified felt electrode is illustrated in Figure 13 and the results of peak separation and the peak current ratio for this couple, including the acid-first baseline, are reported in Table 17.

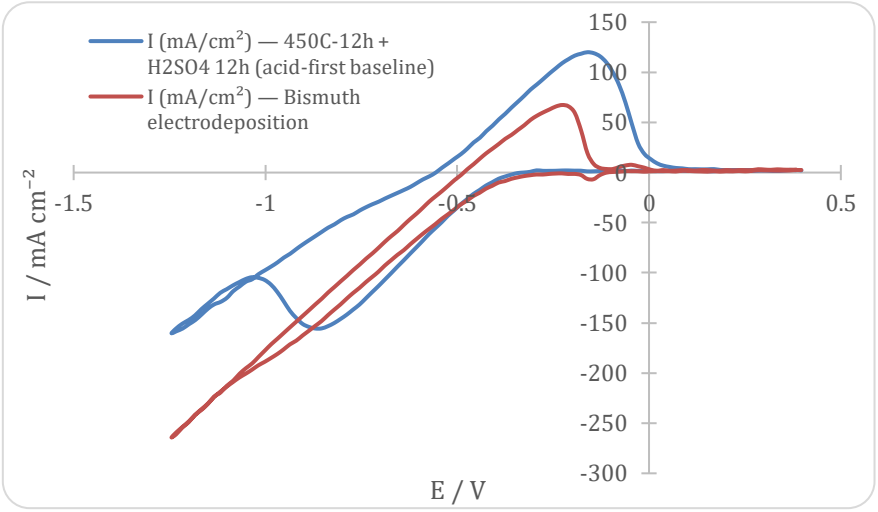


Figure 13: Cyclic voltammograms of the V^{2+}/V^{3+} couple, bismuth-electrodeposited electrode vs. acid-first baseline

Table 17: CV peak separation and peak current ratio for the V^{2+}/V^{3+} couple, bismuth-electrodeposited electrodes vs. acid-first baseline

Sample	ΔEp (mV)	ipa/ipc (raw)
450 °C-12 h + H_2SO_4 12 h (acid-first baseline)	726	0.765
Bismuth electrodeposition	790	0.317

Regarding the V^{2+}/V^{3+} couple, the performance of the bismuth-modified electrode was substantially worse than the acid-first baseline. Peak separation increased from the acid-first baseline value of 726 mV to 790 mV, and the peak current ratio decreased from 0.765 to 0.317, which is significantly lower than the expected value of 1.0 for a fully reversible system. This is directly illustrated in Figure 13.

4.5.2. EIS Results

The Nyquist spectra for the flow cells assembled with negative electrode felt modified by bismuth electrodeposition is compared with the acid-first baseline in Figure 14; the R_s and R_{ct} values are provided in Table 18.

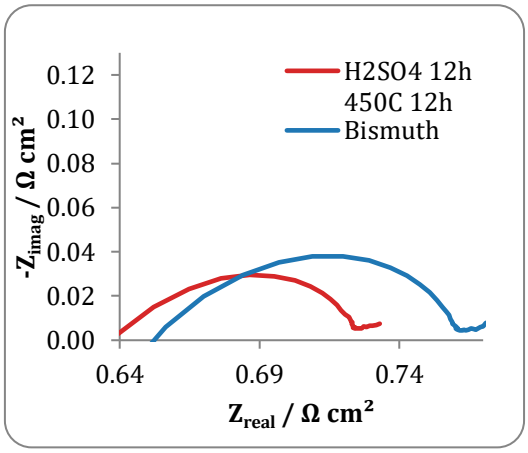


Figure 14: Nyquist plots, bismuth-electrodeposited electrode vs. acid-first baseline

Table 18: EIS-derived ohmic and charge-transfer resistance for bismuth-electrodeposited electrodes vs. acid-first baseline

Sample	R_s (Ω cm²)	R_{ct} (Ω cm²)
450 °C-12 h + H_2SO_4 12 h (acid-first baseline)	0.64	0.084
Bismuth electrodeposition	0.656	0.108

The R_{ct} was found to be higher in the case of a cell with a bismuth-modified electrode. This increase is contrary to the reduction expected from an effective electrocatalyst. Additionally, the R_s of the bismuth electrode was similar to that of the acid-first baseline, indicating that bismuth did not measurably impact bulk or contact resistance.

4.5.3. Polarization results

The polarization and power density curves are presented in Figure 15 and the metrics derived from the polarization curves are provided in Table 19.

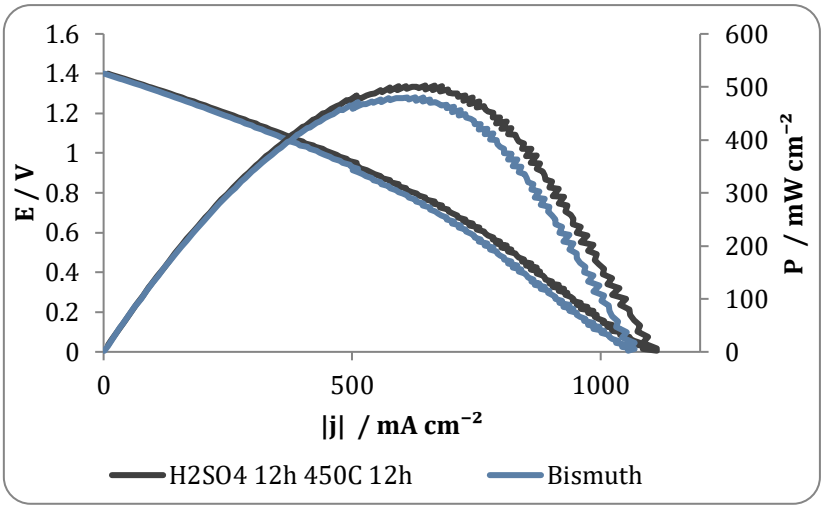


Figure 15: Polarization and power-density curves, bismuth-electrodeposited electrode vs. acid-first baseline

Table 19: Polarization metrics for bismuth-electrodeposited electrodes vs. acid-first baseline

Sample	Max Pd (mW cm^{-2})	Limiting *j* (mA cm^{-2})
450 ºC-12 h + H_2SO_4 12 h (acid-first baseline)	502.6	1112.9
Bismuth electrodeposition	480.3	1068.3

Full-cell performance was relatively similar under both conditions. Peak power density of a cell with bismuth-modified electrode (480.3 mW cm^{-2}) was 5% lower than the baseline (502.6 mW cm^{-2}). The current density was also lower (1068.3 *vs.* 1112.9 mA cm^{-2}), consistent with the decreased kinetics derived from EIS and CV, though the reduction was small relative to the half-cell changes. The pronounced kinetic penalty at the negative electrode had a modest impact on full-cell polarization.

4.5.4. Battery cycling performance

Cycling performance was evaluated at 150 mA cm^{-2}, efficiencies are reported in Table 20.

Table 20: Cycling performance of cells with bismuth-electrodeposited electrodes vs. acid-first baseline (150 mA cm^{-2}, reference cycle)

Sample	CE (%)	VE (%)	EE (%)
450 ºC-12 h + H_2SO_4 12 h (acid-first baseline)	99.11	83.26	82.52
Bismuth electrodeposition	82.96	82.77	68.67

Energy efficiency fell substantially after bismuth electrodeposition onto negative electrode, from 82.52 % to 68.67 %. This decline was driven almost entirely by coulombic efficiency, which dropped from 99.11 % to 82.96 %, while voltage efficiency was essentially unchanged (83.26 % vs. 82.77 %). A large CE penalty with VE held constant points to a side reaction or self-discharge process rather than increased ohmic or activation losses.

The cycle-by-cycle data support this. Across the four unflagged cycles, CE for bismuth fell steadily from 83.21 % to 77.00 %, while VE remained stable (82.58–83.21 %) over the same span. A CE that degrades progressively while VE holds steady is consistent with a growing parasitic process at the negative electrode rather than conventional ohmic or structural degradation. The acid-first baseline, by contrast, held CE essentially flat (98.07–99.11 %) across the same four cycles. Data for the cycle by cycle trend can be found in Appendix G - Cycling metrics for battery using Bismuth modified felt.

4.5.5. SEM analysis

Scanning electron microscopy with energy-dispersive X-ray spectroscopy (SEM-EDS) was performed on the bismuth-modified negative-electrode felt to examine the distribution of the deposit across the fiber surface. Figure 16 shows a representative field of the bismuth-modified felt (81.4 × 81.4 µm, panel a) together with a higher-magnification view of a separate deposit region (18.5 × 18.5 µm, panel b).

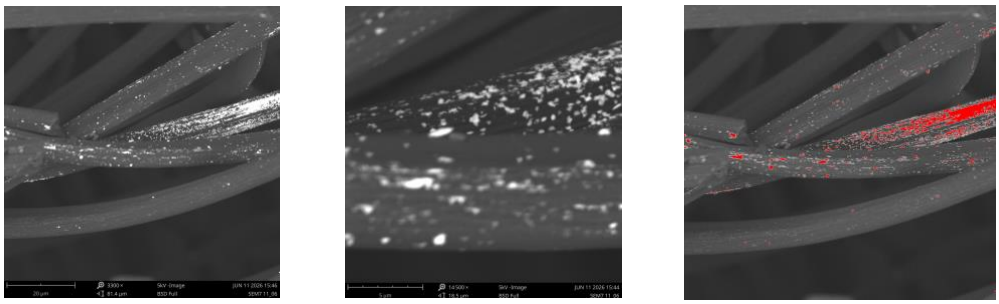


Figure 16: Backscattered-electron micrographs of the bismuth-modified felt. (a) (left) overview, (b) (middle) higher-magnification detail, (c) (right) Threshold overlay (red) of the analysis in Fig. 16(a)

Bismuth was detected by EDX. A spectrum of one of the sites where Bismuth was detected is showed in Appendix H. Bright, high contrast regions correspond to bismuth against the carbon fibre background. The bismuth deposit is localized at discrete sites on the fiber surface rather than forming a continuous conformal coating. The higher-magnification micrograph of a separate deposit region resolves this structure further, showing the deposit to be composed of numerous discrete particles from submicron up to approximately 1 µm, rather than a continuous film.

Taken together, the morphology and point-analysis results show that the electrodeposition protocol produced bismuth coverage concentrated at a small number of nucleation sites, leaving the majority of the fiber surface unmodified. This offers a structural explanation consistent with the electrochemical picture built up: because most of the fiber surface carry no bismuth at all, the felt's bulk ohmic and mass-transport behavior would be expected to remain close to the acid-first baseline, matching the modest polarization and voltage-efficiency changes reported there, while the sparse, exposed bismuth sites might provide a plausible localized origin for the parasitic process implicated in the progressive CE fade.

Across all characterization methods, bismuth electrodeposition underperformed the acid-first baseline at the negative electrode: charge-transfer resistance increased by EIS, V^{2+}/V^{3+} reversibility worsened by CV, and coulombic efficiency declined progressively during cycling in a pattern consistent with a parasitic side reaction rather than ohmic or structural degradation. The bismuth electrodeposition protocol applied here therefore did not deliver the intended catalytic improvement; the acid-first sequence (H_2SO_4-12 h, 450 °C-12 h) remains the leading treatment condition.

4.6. Performance of flow cell with conventional cationic exchange membrane

This section compares the performance of flow cells assembled with anion exchange membrane FAPQ 330, used as the baseline separator throughout the treatment screening above, with the cation exchange membrane Nafion NR-211. Both membranes were tested with felt electrodes prepared using the leading acid-first treatment (H_2SO_4-12 h, 450 °C-12 h), isolating the effect of membrane choice from that of electrode surface treatment

4.6.1. EIS Results

The Nyquist spectra for the cells assembled with different membranes are shown in Figure 17; the R_s and R_{ct} are provided in Table 21.

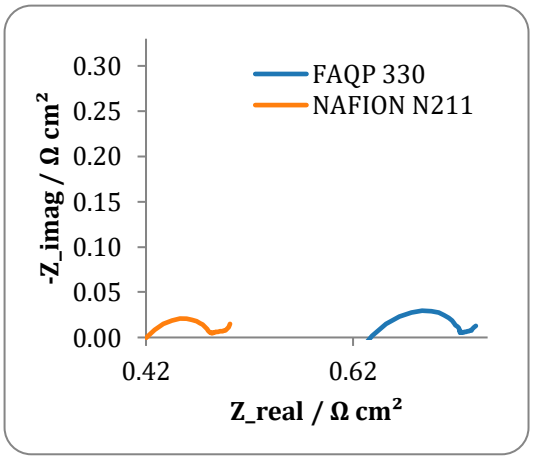


Figure 17: Nyquist plots, FAPQ 330 vs. Nafion NR-211 membranes

Table 21: IS-derived ohmic and charge-transfer resistance, FAPQ 330 vs. Nafion NR-211 membranes

Sample	R_s **(Ω cm²)**	R_{ct} **(Ω cm²)**
450 °C-12 h + H2SO4 12 h, FAPQ 330 (baseline)	0.64	0.08
450 °C-12 h + H2SO4 12 h, Nafion NR-211	0.42	0.06

R_s of a cell with Nafion NR211 membrane is almost 50 % lower than of a cell with FAPQ 330 and is consistent with Nafion's probable higher ionic conductivity compared to the FAPQ 330.

4.6.2. Polarization results

The results of polarization measurements of cells with different membranes are presented in Figure 18, and with the derived metrics are summarized in

Table 22.

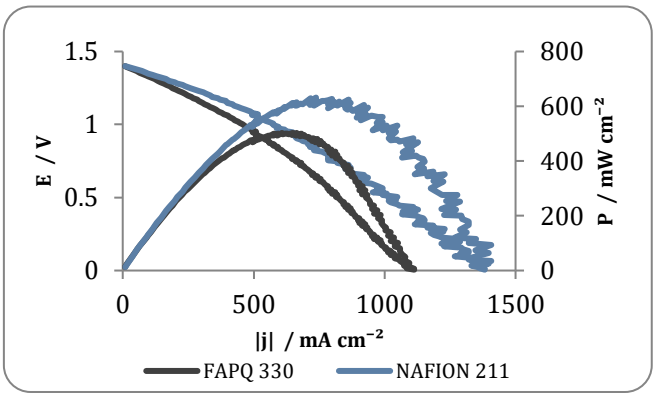


Figure 18: Polarization and power-density curves, FAPQ 330 vs. Nafion NR-211 membranes

Table 22: Polarization metrics, FAPQ 330 vs. Nafion NR-211 membranes

Sample	**Max Pd (mW cm⁻²)**	**Limiting *j* (mA cm⁻²)**
450 °C-12 h + H_2SO_4 12 h, FAPQ 330 (baseline)	502.6	1112.9
450 °C-12 h + H_2SO_4 12 h, Nafion NR-211	631.7	1407.2

A cell with Nafion demonstrated a significant improvement compared to FAPQ 330. This included both an increase of approximately 26 % in peak power density (631.7 *vs.* 502.6 mW cm^{-2}) and in limiting current density of 26.4% (1407.2 vs. 1112.9 mA cm^{-2}).

4.6.3. Battery cycling performance

Results of charge-discharge performance are presented in Table 23:

Table 23: Cycling performance, FAPQ 330 vs. Nafion NR-211 membranes (150 mA cm^{-2}, reference cycle)

Sample	**CE (%)**	**VE (%)**	**EE (%)**
450 ºC-12 h + H_2SO_4 12 h, FAPQ 330 (baseline)	99.11	83.26	82.52
450 ºC-12 h + H_2SO_4 12 h, Nafion NR-211	96.07	86.68	83.28

The cell with FAPQ 330 demonstrated a coulombic efficiency (CE) of 99.11 %, and Nafion showed a CE of 96.07 %. The lower CE of the cell with Nafion might be caused by the more intense crossover through it in comparison with the anionic exchange membrane, however, this needs to be verified in separate crossover studies. However, the lower CE of Nafion was counterbalanced by its higher voltage efficiency consistent with its lower ohmic resistance compared with FAPQ. Together, this resulted in a greater energy efficiency of Nafion at 83.28 % compared to FAPQ 330, which had an energy efficiency of 82.52 %.

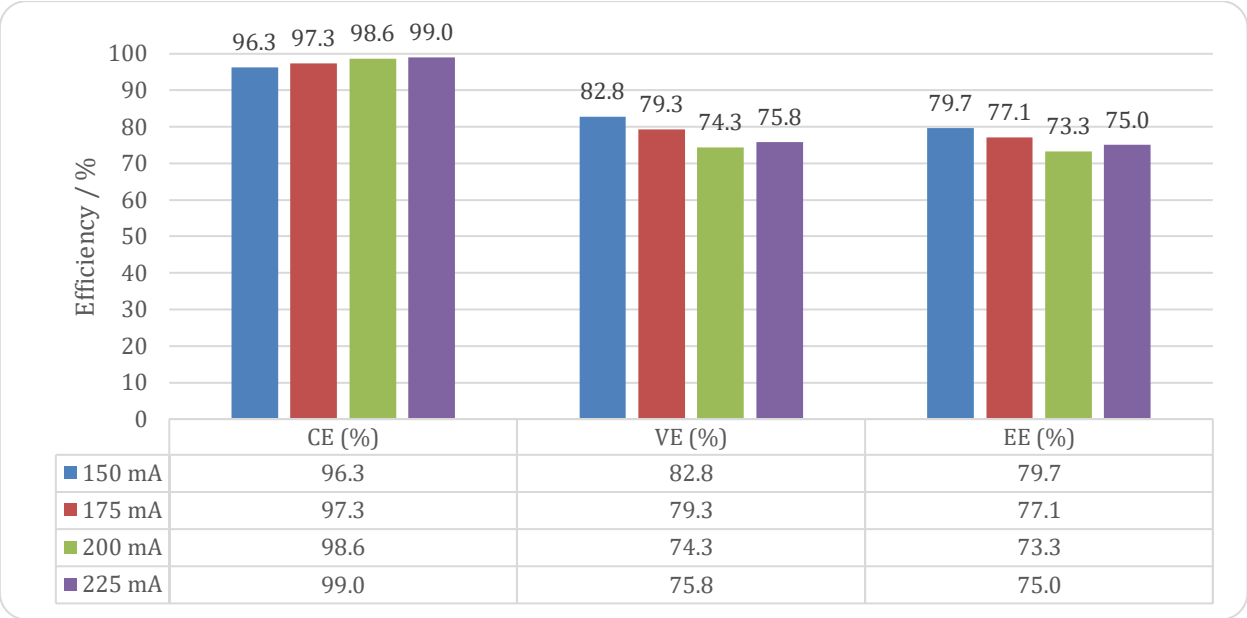
In the long-term tests performed with the Nafion membrane (16 cycles), CE remains tight and stable (95.8–96.1 %, no drift), while VE declines slowly and steadily from 86.9 % at cycle 2 to 86.1 % at cycle 17. This is a gradual, monotonic decline rather than a step change, consistent with progressive rather than catastrophic degradation over extended cycling. EE tracks VE down accordingly, from 83.3 % to 82.5 %, notably, still at or above the FAPQ 330 reference-cycle value (82.52 %, the 3rd cycle) even after 16 cycles.

4.7. Upscaling

The main objective of this work was a development of effective and simple treatment procedure for the carbon felt electrodes to improve the performance of a vanadium flow cell. Most of the experimental work was performed in a laboratory-scale flow cell equipped with 4 cm^2 electrodes.

Following the development of the electrode treatment procedure at this scale, the optimized protocol was transferred to a larger electrode format with an active area of 20 cm^2.

These upscaling tests were conducted in a commercial Pinflow cell (Czech Republic) using a FAPQ-330 membrane, selected due to its low-fluorinated composition as a more sustainable alternative to conventional fully fluorinated membranes. Cycles were performed at 150, 175, 200 and 225 mA cm^{-2}. The results are listed in Figure 19:



	CE (%)	VE (%)	EE (%)
150 mA	96.3	82.8	79.7
175 mA	97.3	79.3	77.1
200 mA	98.6	74.3	73.3
225 mA	99.0	75.8	75.0

Figure 19: Cycling performance of acid-first-treated electrodes at 20 cm² scale, 150-225 mA cm⁻², Pinflow cell

The scale up to 20 cm^2 resulted in cell EE of 79.7 % at a current density of 150 mA cm^{-2}, for the reference cycle.

CE increased with increasing current density. At higher current densities, the vanadium ion crossover across the membrane is less pronounced, resulting in higher CE [12]. VE decreased with increasing current density. The higher applied current increases the ohmic contribution to the cell voltage, widening the gap between the charge and discharge voltage profiles and reducing VE.

5. Conclusions

In this work, several modification approaches were explored to improve the performance of carbon felt electrodes in a VRFB. These included acidic, thermal, and plasma treatments, chemical modification with bismuth particles, and propylene conditioning. Treatments were evaluated in terms of effects on the conductivity under compression, electrochemical activity toward the target redox reactions, and felt morphology. Results were then correlated with full-cell performance by analyzing R_s and R_{ct}, power and current densities, and CE, VE and EE.

The thermal treatment in the temperature range of 400 to 600 °C resulted in a noticeable effect on the conductivity of the stacked assembly of two felts between bipolar plates. The felt samples treated at 450 °C for 12 h exhibited the highest conductivity; the decrease in conductivity after higher-temperature treatment suggests rather aggressive oxidation of the fiber structure, disrupting conductive pathways. Treatment at moderate temperatures (400–450 °C), reduced R_s and R_{ct} and consequently improved the VE and CE within the series of felts. Based on the EIS analysis and charge–discharge performance results, the effect of treatment duration at 450 °C was investigated, and a 12 h treatment was identified as the optimal thermal activation procedure. The cell assembled with the optimally treated felt electrodes and a FAPQ330 membrane achieved a target energy efficiency of 80.09 % at a current density of 150 mA cm^{-2}.

In order to improve performance further, acidic treatment prior to thermal was applied. Based on the CV, it can be concluded that acid treatment for more than 3 h improves electrode kinetics compared to solely thermal treatment. Using optimum felt treatment conditions (12 h in H_2SO_4, 450 °C for 12 h), the superior cell performance in the series was achieved: CE of 99.11 %, VE of 83.26 % and EE of 82.52 % at a current density of 150 mA cm^{-2} (FAPQ330).

The treatment in nitrogen plasma, although allowing to decrease the R_s of thermally treated felts, deteriorated the kinetics due to increased R_{ct}. As a result, the plasma-treated samples did not outperform the thermal or acidic/thermal treatments in this work.

The additional conditioning of thermally treated felt samples in propylene and the surface modification by bismuth electrodeposition did not improve the performance of the electrodes in flow cells. In both cases, the treatments resulted in increase of R_s and R_{ct}, deteriorated the reversibility in V(II)/V(III) redox pairs and decreased the cell performance metrics.

For comparison, several tests were run with Nafion NR211 membrane instead of the anion exchange FAPQ membrane. Although the cell with NR211 showed lower CE (96.07 *vs.* 99.11 % vs. for the FAPQ330), it overperformed in VE due to lower ohmic losses in the cell, as confirmed by EIS, resulting in slightly higher VE of 83.28 % against 82.52 % for FAPQ330.

Finally, the treatment was upscaled from 4 cm^2 to a 20 cm^2 flow cell using the best-performing felt electrodes and a FAPQ 330 membrane, resulting in an EE of 79.7 % at 150 mA cm^{-2}. Overall, this work presented guidelines for developing high-performing carbon-felt electrodes for VRFBs.

A valuable direction for future work would be a full surface characterization of the treated electrodes, to better understand the actual chemical and structural changes each treatment introduces on the felt surface. Techniques such as X-ray photoelectron spectroscopy (XPS) could quantify the density and type of oxygen- and nitrogen-containing functional groups generated by each treatment, complementing the SEM imaging already carried out and providing a more direct link between treatment conditions and the electrochemical performance observed.

It would also be of interest to study how treatment-induced properties evolve over time, since the stability of surface functionalization and wettability under prolonged storage or cycling is critical for practical deployment. A systematic aging study, tracking felt conductivity, wettability, and electrochemical activity over weeks to months, would clarify whether the gains achieved by the acid-first treatment persist over the operational lifetime of a VRFB system.

6. Assessment of the work done

6.1. Objectives Achieved

This dissertation aimed to evaluate how surface treatments affect the performance of carbon felt electrodes in vanadium redox flow batteries, and to link treatment, felt properties, and cell performance. This was achieved: an acid-first sequence (H_2SO_4, 12 h; 450 °C, 12 h) was identified as the leading treatment, raising reference-cycle energy efficiency from 80.09 % (thermal only) to 82.52 % at 150 mA cm^{-2}, presumably by opening the felt's pore structure ahead of thermal functionalization. Further modifications tested on this baseline, plasma, propylene conditioning, bismuth electrodeposition, and an alternating sequence, all reduced performance, while pairing the acid-first felt with a Nafion NR-211 membrane raised efficiency to 83.28 %. The treatment was transferred to a 20 cm^2 commercial cell across and presented high performance across 150-225 mA cm^{-2} (EE of 79.7 % at 150 mA cm^{-2}, 77.1 % at 175 mA cm^{-2}, 73.3 % at 200 mA cm^{-2}, and 75.0 % at 225 mA cm^{-2}).

6.2. Contribution to the Sustainable Development Goals

Table 24: Contribution to the Sustainable Development Goals

SDG (Target)	Contribution	Indicator
7 – Affordable and Clean Energy (7.2, 7.a)	Higher-efficiency electrodes support cost-effective, long-duration storage for renewable integration	EE: 80.1 %→82.5 % (acid-first), 83.3 % (+Nafion), 150 mA cm^{-2}
9 – Industry, Innovation and Infrastructure (9.5)	Systematic treatment comparison and scale-up on a commercial electrode format	EE: 79.7 % (150 mA cm^{-2}) to 73.3 % (200 mA cm^{-2}) maintained across the 4→20 cm^2 scale-up
12 – Responsible Consumption and Production (12.2)	Scale-up validated with a low-fluorinated membrane (FAPQ 330), avoiding a fully fluorinated alternative	Full-scale demonstration used FAPQ 330 exclusively

6.3. Final Assessment

I believe this project was successful. Most changes that went beyond the acid-first baseline and that we explored tended to either reduce performance or leave it unchanged. In the absence of obvious positive results, finding out which changes truly improved performance was helpful. The acid-first approach combines several different methods into a single answer, and

although most of the project is spent measuring parts of this answer, combining as many methods as possible was the most valuable part of the project.

7. References

[1] "28 April 2025 Blackout." Accessed: Mar. 13, 2026. [Online]. Available: https://www.entsoe.eu/publications/blackout/28-april-2025-iberian-blackout/

[2] "Storm Kristin – Government statement." Accessed: Mar. 13, 2026. [Online]. Available: https://www.portugal.gov.pt/en/gc25/communication/news-item?i=storm-kristin-government-statement

[3] "Davos 2026: Special address by Mark Carney, PM of Canada," World Economic Forum. Accessed: Mar. 13, 2026. [Online]. Available: https://www.weforum.org/stories/2026/01/davos-2026-special-address-by-mark-carney-prime-minister-of-canada/

[4] X. Luo, J. Wang, M. Dooner, and J. Clarke, "Overview of current development in electrical energy storage technologies and the application potential in power system operation," *Applied Energy*, vol. 137, pp. 511–536, Jan. 2015, doi: 10.1016/j.apenergy.2014.09.081.

[5] V. Mahadevan, S. R. S, M. A. Rusho, and S. Yishak, "Critical review of energy storage systems: A comparative assessment of mechanisms, advantages, challenges, and integration with renewable energy," *Results in Engineering*, vol. 26, p. 105589, Jun. 2025, doi: 10.1016/j.rineng.2025.105589.

[6] A. G. Olabi, C. Onumaegbu, T. Wilberforce, M. Ramadan, M. A. Abdelkareem, and A. H. Al – Alami, "Critical review of energy storage systems," *Energy*, vol. 214, p. 118987, Jan. 2021, doi: 10.1016/j.energy.2020.118987.

[7] T. Jiang, D. Shen, Z. Zhang, H. Liu, G. Zhao, Y. Wang, S. Tan, R. Luo, and W. Chen, "Battery technologies for grid-scale energy storage," *Nat. Rev. Clean Technol.*, vol. 1, no. 7, pp. 474–492, Jun. 2025, doi: 10.1038/s44359-025-00067-9.

[8] A. A. Kebede, T. Kalogiannis, J. Van Mierlo, and M. Berecibar, "A comprehensive review of stationary energy storage devices for large scale renewable energy sources grid integration," *Renewable and Sustainable Energy Reviews*, vol. 159, p. 112213, May 2022, doi: 10.1016/j.rser.2022.112213.

[9] I. Iwakiri, T. Antunes, H. Almeida, J. P. Sousa, R. B. Figueira, and A. Mendes, "Redox Flow Batteries: Materials, Design and Prospects," *Energies*, vol. 14, no. 18, p. 5643, Sep. 2021, doi: 10.3390/en14185643.

[10] A. Z. Weber, M. M. Mench, J. P. Meyers, P. N. Ross, J. T. Gostick, and Q. Liu, "Redox flow batteries: a review," *J Appl Electrochem*, vol. 41, no. 10, pp. 1137–1164, Oct. 2011, doi: 10.1007/s10800-011-0348-2.

[11] M. Skyllas-Kazacos and F. Grossmith, "Efficient Vanadium Redox Flow Cell," *J. Electrochem. Soc.*, vol. 134, no. 12, pp. 2950–2953, Dec. 1987, doi: 10.1149/1.2100321.

[12] R. Monteiro, J. Leirós, M. Boaventura, and A. Mendes, "Insights into all-vanadium redox flow battery: A case study on components and operational conditions," *Electrochimica Acta*, vol. 267, pp. 80–93, Mar. 2018, doi: 10.1016/j.electacta.2018.02.054.

[13] J. Mitali, S. Dhinakaran, and A. A. Mohamad, "Energy storage systems: a review," *Energy Storage and Saving*, vol. 1, no. 3, pp. 166–216, Sep. 2022, doi: 10.1016/j.enss.2022.07.002.

[14] B. Dunn, H. Kamath, and J.-M. Tarascon, "Electrical Energy Storage for the Grid: A Battery of Choices," *Science*, vol. 334, no. 6058, pp. 928–935, Nov. 2011, doi: 10.1126/science.1212741.

[15] L. Eifert, R. Banerjee, Z. Jusys, and R. Zeis, "Characterization of Carbon Felt Electrodes for Vanadium Redox Flow Batteries: Impact of Treatment Methods," *J. Electrochem. Soc.*, vol. 165, no. 11, pp. A2577–A2586, 2018, doi: 10.1149/2.0531811jes.

[16] X. Li, T. Ye, X. Meng, D. He, L. Li, K. Song, J. Jiang, and C. Sun, "Advances in the Application of Sulfonated Poly(Ether Ether Ketone) (SPEEK) and Its Organic Composite Membranes for

Proton Exchange Membrane Fuel Cells (PEMFCs)," *Polymers*, vol. 16, no. 19, p. 2840, Oct. 2024, doi: 10.3390/polym16192840.

[17] T. X. Huong Le, M. Bechelany, and M. Cretin, "Carbon felt based-electrodes for energy and environmental applications: A review," *Carbon*, vol. 122, pp. 564–591, Oct. 2017, doi: 10.1016/j.carbon.2017.06.078.

[18] K. J. Kim, Y.-J. Kim, J.-H. Kim, and M.-S. Park, "The effects of surface modification on carbon felt electrodes for use in vanadium redox flow batteries," *Materials Chemistry and Physics*, vol. 131, no. 1–2, pp. 547–553, Dec. 2011, doi: 10.1016/j.matchemphys.2011.10.022.

[19] N. Aguiló-Aguayo, T. A. Ebert, R. Amade, E. Bertran, R. Ospina, J. Rodriguez-Pereira, C. Ponce De León, T. Bechtold, and T. Pham, "Comparative Analysis of Thermal Activation on Felts and Continuous Carbon Filament Electrodes for Vanadium Redox Flow Batteries," *ChemElectroChem*, vol. 11, no. 21, p. e202400417, Nov. 2024, doi: 10.1002/celc.202400417.

[20] A. Kaur, K. Il Jeong, S. Su Kim, and J. Woo Lim, "Optimization of thermal treatment of carbon felt electrode based on the mechanical properties for high-efficiency vanadium redox flow batteries," *Composite Structures*, vol. 290, p. 115546, Jun. 2022, doi: 10.1016/j.compstruct.2022.115546.

[21] P. Mazúr, J. Mrlík, J. Beneš, J. Pocedič, J. Vrána, J. Dundálek, and J. Kosek, "Performance evaluation of thermally treated graphite felt electrodes for vanadium redox flow battery and their four-point single cell characterization," *Journal of Power Sources*, vol. 380, pp. 105–114, Mar. 2018, doi: 10.1016/j.jpowsour.2018.01.079.

[22] G. Dai, Y. Huang, F. Chu, C. Jin, and H. Liu, "Analysis of the effect of thermal treatment and catalyst introduction on electrode performance in vanadium redox flow battery," *Heliyon*, vol. 10, no. 13, p. e33561, Jul. 2024, doi: 10.1016/j.heliyon.2024.e33561.

[23] M. Rahimi, F. Fenini, and A. Bentien, "Optimizing the thermal treatment procedure using electrochemical methods to improve the performance of vanadium redox flow batteries," *Journal of Power Sources Advances*, vol. 33, p. 100180, Jun. 2025, doi: 10.1016/j.powera.2025.100180.

[24] M. Schilling, L. Eifert, K. Köble, M. Jaugstetter, N. Bevilacqua, K. F. Fahy, K. Tschulik, A. Bazylak, and R. Zeis, "Investigating the Influence of Treatments on Carbon Felts for Vanadium Redox Flow Batteries," *ChemSusChem*, vol. 17, no. 1, p. e202301063, Jan. 2024, doi: 10.1002/cssc.202301063.

[25] A. Hassan and T. Tzedakis, "Enhancement of the electrochemical activity of a commercial graphite felt for vanadium redox flow battery (VRFB), by chemical treatment with acidic solution of K2Cr2O7," *Journal of Energy Storage*, vol. 26, p. 100967, Dec. 2019, doi: 10.1016/j.est.2019.100967.

[26] C. Ding, Z. Shen, Y. Zhu, and Y. Cheng, "Insights into the Modification of Carbonous Felt as an Electrode for Vanadium Redox Flow Batteries," *Materials (Basel)*, vol. 16, no. 10, p. 3811, May 2023, doi: 10.3390/ma16103811.

[27] D. Dixon, D. J. Babu, J. Langner, M. Bruns, L. Pfaffmann, A. Bhaskar, J. J. Schneider, F. Scheiba, and H. Ehrenberg, "Effect of oxygen plasma treatment on the electrochemical performance of the rayon and polyacrylonitrile based carbon felt for the vanadium redox flow battery application," *Journal of Power Sources*, vol. 332, pp. 240–248, Nov. 2016, doi: 10.1016/j.jpowsour.2016.09.070.

[28] T. Jirabovornwisut, B. Singh, A. Chutimasakul, J.-H. Chang, J.-Z. Chen, A. Arpornwichanop, and Y.-S. Chen, "Characteristics of Graphite Felt Electrodes Treated by Atmospheric Pressure Plasma Jets for an All-Vanadium Redox Flow Battery," *Materials*, vol. 14, no. 14, p. 3847, Jul. 2021, doi: 10.3390/ma14143847.

[29] A. J. Bard and L. R. Faulkner, *Electrochemical methods: fundamentals and applications*, 2nd ed. New York: Wiley, 2001.

[30] D. Aaron, Z. Tang, A. B. Papandrew, and T. A. Zawodzinski, "Polarization curve analysis of all-vanadium redox flow batteries," *J Appl Electrochem*, vol. 41, no. 10, pp. 1175–1182, Oct. 2011, doi: 10.1007/s10800-011-0335-7.

[31] L. Eifert, Z. Jusys, R. J. Behm, and R. Zeis, "Side reactions and stability of pre-treated carbon felt electrodes for vanadium redox flow batteries: A DEMS study," *Carbon*, vol. 158, pp. 580–587, Mar. 2020, doi: 10.1016/j.carbon.2019.11.029.

[32] S.-K. Park, J. Shim, J. H. Yang, C.-S. Jin, B. S. Lee, Y.-S. Lee, K.-H. Shin, and J.-D. Jeon, "The influence of compressed carbon felt electrodes on the performance of a vanadium redox flow battery," *Electrochimica Acta*, vol. 116, pp. 447–452, Jan. 2014, doi: 10.1016/j.electacta.2013.11.073.

[33] S. Chen, C. Sun, H. Zhang, H. Yu, and W. Wang, "Electrochemical Deposition of Bismuth on Graphite Felt Electrodes: Influence on Negative Half-Cell Reactions in Vanadium Redox Flow Batteries," *Applied Sciences*, vol. 14, no. 8, p. 3316, Apr. 2024, doi: 10.3390/app14083316.

[34] F. Hasan, V. Mahanta, and A. A. A. Abdelazeez, "Quinones for Aqueous Organic Redox Flow Battery: A Prospective on Redox Potential, Solubility, and Stability," *Adv Materials Inter*, vol. 10, no. 24, p. 2300268, Aug. 2023, doi: 10.1002/admi.202300268.

[35] C. He, Y. Zhang, S. Zhang, X. Peng, J. Noack, M. Skyllas-Kazacos, L. Wang, and B. Luo, "Aqueous iron-based redox flow batteries for large-scale energy storage," *National Science Review*, vol. 12, no. 7, p. nwaf218, Jun. 2025, doi: 10.1093/nsr/nwaf218.

[36] A. Mahmood, Z. Zheng, and Y. Chen, "Zinc–Bromine Batteries: Challenges, Prospective Solutions, and Future," *Advanced Science*, vol. 11, no. 3, p. 2305561, Jan. 2024, doi: 10.1002/advs.202305561.

[37] E. Sánchez-Díez, E. Ventosa, M. Guarnieri, A. Trovò, C. Flox, R. Marcilla, F. Soavi, P. Mazur, E. Aranzabe, and R. Ferret, "Redox flow batteries: Status and perspective towards sustainable stationary energy storage," *Journal of Power Sources*, vol. 481, p. 228804, Jan. 2021, doi: 10.1016/j.jpowsour.2020.228804.

[38] R. S. Nicholson and I. Shain, "Theory of Stationary Electrode Polarography".

Appendix A - Comparison of Energy Storage Technologies

Table 25: Comparison of energy storage technologies by key performance metrics [5], [7], [8]

Technology	Energy Density (Wh/kg)	Energy Density (kWh/m³)	Cycle Life	Round-trip Efficiency (%)	Self-discharge Rate	Maturity	Typical Applications
PHS	—	0.5–1.5	>40 years	<80 %	Negligible	Fully commercialized	Long-duration & seasonal storage, peak shaving
CAES	—	3–6	~40 years	42–75 %[a]	Negligible	Mature/commercializing	Long-duration storage, peak shaving
Li-ion	80–200	—	1,000–10,000	85–97 %	~0.1 %/day	Mature, dominant commercial	Renewables integration, peak shaving, frequency regulation
Lead-acid	30–50	—	300–1,500	75–85 %	<0.3 %/day	Fully commercial	Backup power, UPS, black start
Na-S	150–240	—	4,500–15,000	80–90 %	~0.1 %/day	Commercial	Grid-scale long-duration, peak shaving
Vanadium RFB	10–50	—	5,000–20,000	65–85 %	Negligible (idle)	Early/growing commercial	Long-duration storage, renewables integration
Supercapacitors	~5	—	>500,000	~90 %	~40 %/day	Commercial/demonstration	Frequency regulation, power quality, UPS

[a] CAES efficiency varies substantially by configuration: conventional diabatic CAES reaches roughly 42–53 % due to heat loss during reheating, while isothermal CAES reaches 70–75 % by recovering compression heat; Jiang et al. (2025) independently report CAES efficiency generally below 65.

Appendix B - Comparison of non-vanadium redox flow battery chemistries

Table 26: Comparison of non-vanadium redox flow battery chemistries [7], [9], [10], [34], [35], [36], [37]

Parameter	**Iron-Chromium**	**Zinc-Bromine**	**Organic (quinone-based)**	**Iron**
Chemistry	Fe^{3+}/Fe^{2+} (+), Cr^{3+}/Cr^{2+} (−)	Br_2/Br^- (+), Zn^{2+}/Zn (−)	Varies by quinone derivative	Fe^{3+}/Fe^{2+} (+, in solution), Fe^0/Fe^{2+} (−, plated/stripped)
Cell voltage	~1.18 V	~1.8 V	Typically < 1.2 V	1.26 V at 50 % SoC
Energy density	10–35 Wh kg^{-1}	30–65 Wh L^{-1}	Comparable to or below vanadium; under active improvement	76 Wh L^{-1} (theoretical, 0.5 kg L^{-1} $FeCl_2$)
Benefits	Low-cost, abundant active materials	High cell voltage and energy density relative to other non-vanadium systems; cost-effective	Metal-free; tunable redox potential; can use carbon-steel tanks (mildly alkaline chemistry)	Abundant, inexpensive material (electrolyte ≈3 % of total cost); non-toxic
Problems	Slow Cr^{3+}/Cr^{2+} kinetics; membrane crossover and capacity fade	Zinc dendrite formation; bromine toxicity and crossover	Limited long-term molecular stability; difficulty reaching competitive cell voltage	pH-sensitive electrochemistry; HER promotes $Fe^{2+}/Fe(OH)_3$ precipitation; requires daily anolyte pH maintenance
Commercialisation status	Demonstration stage	Commercial in a hybrid (non-flow) form; flow variants at small commercial/demonstration scale	Pre-commercial; pilot-scale demonstrations underway	Commercialized

Companies[1]	Redox One; Saudi Aramco (hybrid Fe–V variant)	Primus Power; Eos Energy (hybrid zinc system)	Quino Energy (partnering with Jena Batteries for hardware)	ESSC (50 kW/400 kWh, >20,000 cycles); Energy Fuel® (10 kW pilot 2016, 100 kW field demo 2017, targeting MW-scale)

[1]Company and commercialization information current as of early 2026, based on public company materials and industry reporting

Appendix C - Parameter tables for 4.65EA Sigracell felt and FAPQ 330 and Nafion 211 membranes

Table 27: Physical properties of SGL Sigracell GFD 4.65 EA carbon felt

Property	**GFD 4.65 EA**
Areal weight (g m^{-2})	**465 g m^{-2}**
Thickness, uncompressed (mm)	**4.6 mm**
Porosity (%)	94 %
Material	PAN-based carbon felt

Table 28: Specifications of the FAPQ 330 and Nafion NR-211 membranes

Property	**FAPQ 330**	**Nafion NR-211**
Type	Anion exchange membrane	Cation exchange membrane
Manufacturer	Fumatech, Germany	Chemours/ Ion Power GmbH
Thickness (µm)	30	25.4
Ion exchange capacity (meq g^{-1})	-	0.95–1.01
Functional group	-	Sulfonic acid (–SO_3^-)

Appendix D - SEM Micrographs of Untreated and Treated Carbon Felt Electrodes

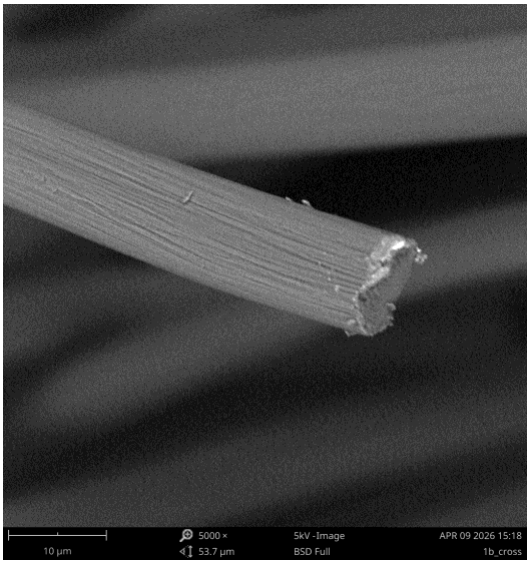


Figure 21: SEM micrograph of the thermal-only treated carbon felt (450 ºC / 12 h)

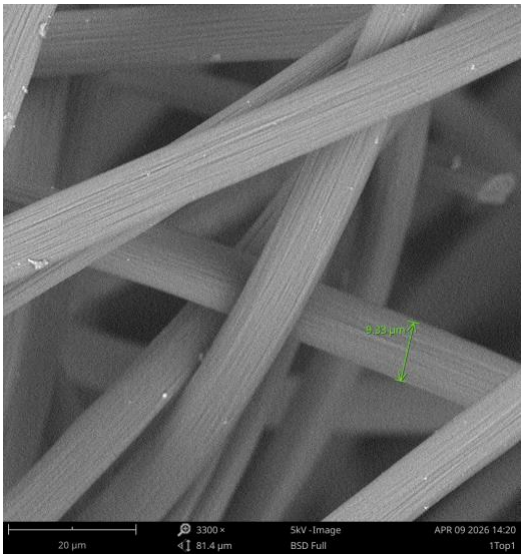


Figure 20: SEM micrograph of the untreated carbon felt

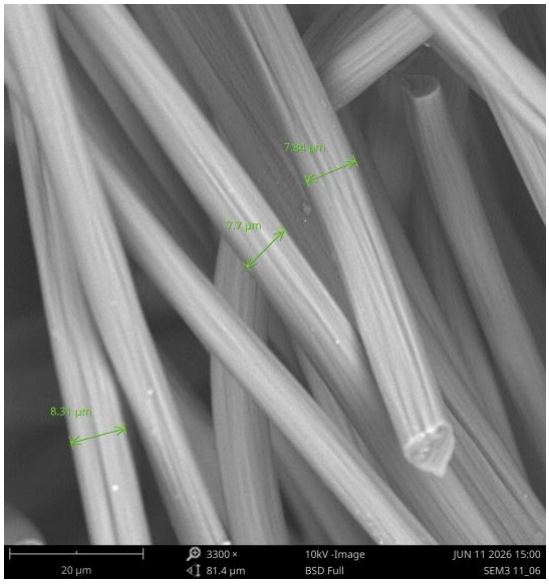


Figure 22: SEM micrograph of the acid-first treated carbon felt (H_2SO_4 / 12 h - 450 ºC / 12 h)

Appendix E - Consolidated Cycling Performance Across All Treatment Conditions

Table 29: Mean Coulombic, voltage, and energy efficiencies (cycles 2–5) across all treatment conditions tested (150 mA cm $^{-2}$)

Sample / Condition	**N cycles used**	**Mean CE, cyc. 2-5 (%)**	**Mean VE, cyc. 2-5 (%)**	**Mean EE, cyc. 2-5 (%)**
H_2SO_4 / 12 h - 400 °C / 12 h	4	98.31	82.09	80.70
400 °C / 12 h	4	96.21	81.97	78.87
450 °C / 12+12 h	4	95.63	82.11	78.52
450 °C / 12 h	4	93.96	83.80	78.73
H_2SO_4 / 3 h - 450 °C / 12 h	4	97.98	81.57	79.92
H_2SO_4 / 7 h - 450 °C / 12 h	4	98.12	81.92	80.38
450 °C / 6 h	4	82.48	78.76	64.97
H_2SO_4 / 12 h - 450 °C / 12 h	4	98.68	83.24	82.14
450 °C / 12 h - propylene	4	95.49	82.11	78.41
450 °C / 12 h - plasma 10 min	4	97.20	78.27	76.08
H_2SO_4 / 18 h - 450 °C / 12 h	4	95.40	83.74	79.89
450 °C / 12 h - plasma 3 min	4	91.76	78.37	71.91
500 °C / 12 h	4	96.62	68.67	66.36
500 °C / 3 h	4	81.40	81.43	66.29
600 °C / 0.5 h	4	95.53	80.15	76.56
Bismuth deposition	4	80.36	82.92	66.62
Nafion membrane	4	96.00	86.70	83.24
Alternating Chemical Thermal	4	95.06	82.45	78.38
Upscale (Pinflow)	4	96.24	82.61	79.50

Appendix F - Python-Based Data Processing Scripts

This appendix documents the custom Python scripts used to convert raw instrument output into the quantitative results reported. Each script is described in a dedicated subsection covering its purpose, computational methods and governing equations.

cv_analysis.py — Cyclic Voltammetry Peak and Charge Analysis

Scan Rate and Electrode Area

Scan rate is taken from the file's instrument-reported slew rate where available; otherwise it is estimated from the data as the median absolute potential step per unit time over the full trace:

$$v = \text{median}\left(\left|\frac{\Delta E}{\Delta t}\right|\right) \tag{C.1}$$

Peak Detection and Baseline Correction

For each branch (anodic or cathodic) of the representative cycle, the current is optionally smoothed with a Savitzky-Golay filter for the purpose of peak detection only; reported peak currents and potentials are always read back from the raw, unsmoothed data at the detected index.

Where baseline correction is enabled, a linear baseline is fitted through the mean potential and current of a short window immediately before and immediately after a provisional peak location, following the foot-to-foot method described by Bard and Faulkner (2001, Electrochemical Methods, 2nd ed.) and Nicholson and Shain (1964) [29], [38]:

$$I_{base}(E) = I_0 + \frac{I_1 - I_0}{E_1 - E_0}\,(E - E_0) \tag{C.2}$$

where (E_0, I_0) and (E_1, I_1) are the mean potential and current of the pre-peak and post-peak windows respectively, each window spanning a fixed fraction of the branch length (15 % by default) immediately adjacent to the provisional peak. The corrected current is:

$$I_{corr} = I - I_{base} \tag{C.3}$$

The signal is then searched for peaks using a minimum-prominence and minimum-separation criterion, each scaled to the branch itself where more than one candidate passes the threshold, the one with the largest raw current magnitude is kept. If no candidate passes the prominence threshold, the branch maximum (anodic) or minimum (cathodic) is used instead and the result is flagged as low confidence. The peak current and potential reported by default and every metric derived from them are the raw, uncorrected values at the detected index.

Peak-Derived Metrics

Peak separation:

$$\Delta E_p = E_{pa} - E_{pc} \tag{C.4}$$

Peak current ratio:

$$\left|\frac{i_{pa}}{i_{pc}}\right| \tag{C.5}$$

ΔE_p and the peak current ratio are diagnostic .

Onset Potential

The onset potential for a branch is defined as the first potential, scanning in the direction of that branch, at which the current magnitude exceeds a fixed fraction of the branch's peak current magnitude:

$$E_{onset}\text{: first } E \text{ such that } |I(E)| \geq f_{onset} \cdot |I_{peak}| \tag{C.6}$$

with f_{onset} set to 5 % by default. This is an empirical, threshold-dependent definition common in the electrocatalysis literature rather than a thermodynamically derived quantity; the threshold fraction used should always be reported alongside any onset potential value.

To assess reproducibility within a single file, the same peak-detection procedure (smoothed current, no baseline correction) is applied independently to every complete cycle detected in the file, and the variability of each peak metric across cycles is reported as its standard deviation, with n the number of complete cycles for which that peak was detected:

$$\sigma = \sqrt{\frac{1}{n}\sum_{k=1}^{n}(x_k - \bar{x})^2} \tag{C.7}$$

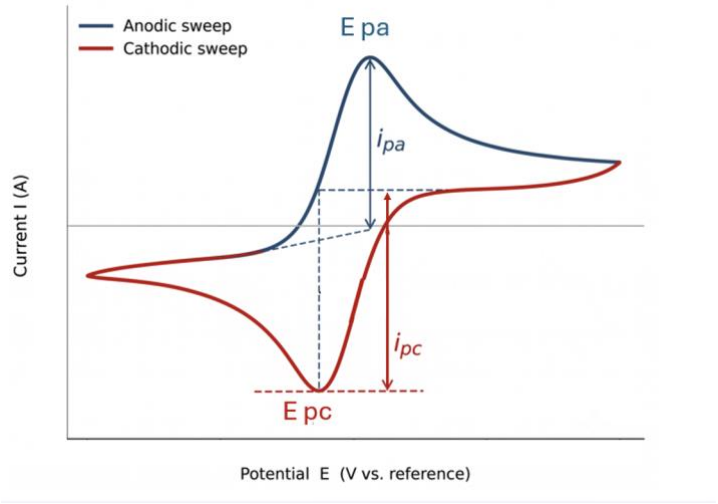


Figure 23: Schematic cyclic voltammogram (illustrative, not measured data) showing the anodic and cathodic peaks and the quantities derived from them. Built using AI tools.

vrfb_cycles.py — Cycling Performance Calculations

Coulombic Efficiency

Charge and discharge capacities, Q_{cha} and Q_{dis}, are taken directly from the log file's reported charge for each half-cycle. Capacities are additionally reported in Ah and mAh (division by 3600 and 3.6 respectively) alongside the native Coulomb values. CE is always computed from the log-reported capacities, independent of whether exact or approximate voltage efficiency is available for the same cycle

Voltage and Energy Efficiency — Approximate (log-based)

Where only the half-cycle summary log is available, voltage efficiency is approximated from the end-of-half-cycle (cutoff) voltages recorded in the log, rather than from a true time-averaged voltage:

$$\mathrm{VE}_{approx} = \frac{V_{dis,end}}{V_{cha,end}} \tag{C.8}$$

$$\mathrm{EE}_{approx} = \mathrm{CE} \times \mathrm{VE}_{approx} \tag{C.9}$$

These values are explicitly labelled as approximate wherever they are reported, and are superseded by the exact values whenever the corresponding timeseries file is available.

Voltage and Energy Efficiency — Exact (timeseries-integrated)

Each segment is integrated numerically to obtain the charge passed and the energy transferred:

$$Q = \sum_i |I_i| \Delta t_i \tag{C.10}$$

$$E = \sum_i V_i \ |I_i| \Delta t_i \tag{C.11}$$

where Δt_i is the sampling interval between consecutive timeseries points (nominally 1 s). E is expressed in watt-seconds and converted to watt-hours by division by 3600. The charge-weighted average half-cycle voltage follows directly:

$$\overline{V} = \frac{E}{Q} \tag{C.12}$$

from which the exact voltage and energy efficiencies are obtained:

$$\mathrm{VE}_{exact} = \frac{\overline{V}_{dis}}{\overline{V}_{cha}} \tag{C.13}$$

$$\mathrm{EE}_{exact} = \frac{E_{dis}}{E_{cha}} \tag{C.14}$$

EE_{exact} is computed directly as the ratio of timeseries-integrated energies and is not algebraically constructed as $\mathrm{CE} \times \mathrm{VE}_{exact}$. Exact values are preferred over the approximate values of wherever available, and every reported table or summary statistic indicates which basis was used.

Anomaly Flagging

Every paired cycle is checked against a fixed set of default criteria (Table 30); a cycle failing any criterion is flagged and, unless configured otherwise, excluded from the summary statistics of while remaining visible in the full per-cycle record.

Table 30: Automatic anomaly-flagging criteria (defaults).

Criterion	**Threshold**	**Effect**
Cycle number	Cycle 1	Excluded from summary statistics (unstable first cycle)
Coulombic efficiency	above 105 %	Flagged as a high-CE anomaly
Coulombic efficiency	below 0 %	Flagged as a negative-CE anomaly
Charge or discharge capacity	below 10 C	Flagged as near-zero capacity
Charge or discharge duration	below 60 s	Flagged as short duration
Log entries for one cycle/half	more than one found	Flagged as duplicate entries; longest duration kept

polarization_analysis.py — Polarization Curve Metrics

Derived Quantities

Current density, signed to match the instrument's own current convention:

$$j = \frac{I}{A} \tag{C.15}$$

Power density, computed pointwise from the signed potential and current and used both directly and in absolute-value form for locating the maximum-power-density point:

$$P_d = \frac{V \cdot I}{A} \tag{C.16}$$

Limiting Current Density

The limiting current density is reported as the current density at the highest-current point actually reached before the sweep ended, j_{lim} = |I|max / A. Two more elaborate detection strategies were evaluated during development and discarded. A numerical-derivative plateau search (restricted to the highest-current 40% of the sweep, thresholded at 5.0 V/A, requiring a 5-point consecutive run) produced false positives on noisy sweeps and, once corrected for noise sensitivity, consistently found no genuine plateau in any condition tested — these cells' polarization curves decline smoothly to voltage collapse with no distinct mass-transport-limited region. A fixed low-voltage cutoff (e.g., 0.05 V) was tried as an alternative but found to be redundant with the sweep's true endpoint, since every measurement is programmed to stop at the same voltage regardless of treatment condition. The maximum recorded value is therefore

reported directly, understood as the empirical endpoint of the measurement protocol rather than a theoretically-derived limiting current.

Appendix G - Cycling metrics for battery using Bismuth modified felt

Table 31:Efficiency metrics for battery using Bi-modified felt

Cycle	CE (%)	VE (%)	EE (%)
2	83.21	82.58	68.71
3	82.96	82.77	68.67
4	78.25	83.12	65.04
5	77.00	83.21	64.07

Appendix H - SEM picture and spectrum for bismuth modified felt

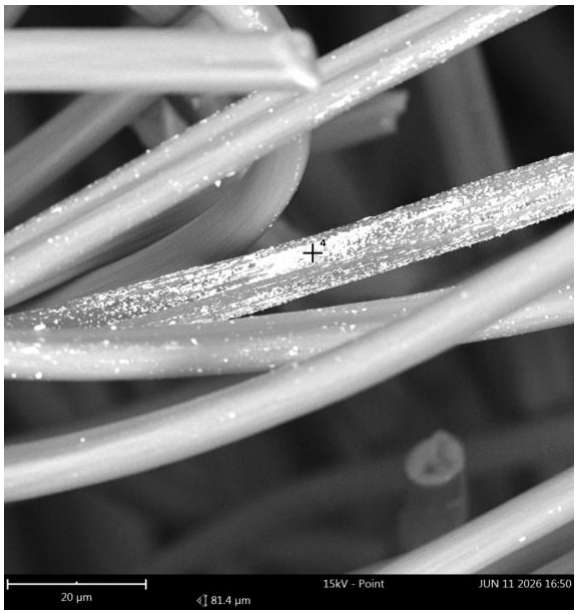


Figure 24: SEM micrograph of the bismuth modified felt surface

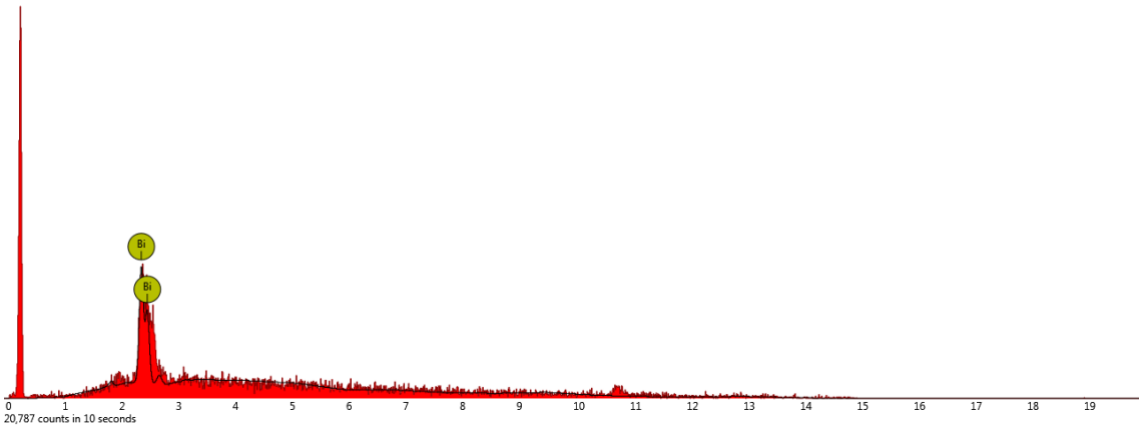


Figure 25: EDX spectrum of the bismuth deposit on the felt surface